Low-level jet height's impact on wind turbine loads: A case study

Fahim Masud Ahmed

Thesis for Master of Science Degree at the
University of Bergen, Norway

2023

Year: 2023
Title: Low-level jet height's impact on wind turbine loads: A case study
Author: Fahim Masud Ahmed

Acknowledgements

I would like to thank my main supervisor Mostafa Bakhoday Paskyabi for his insight, support and help during the writing of this thesis. Without him I would be unaware of the field of low-level jets and wind-induced loading, and this thesis would not be possible.

I would also like to thank my co-supervisors Etienne Cheynet, Marte Godvik and Bruno Antonio Roccia. Their support, knowledge and feedback greatly increased the quality of the thesis, and they provided critical information on which a lot of my knowledge is built upon.

A special thanks goes to the CONWIND-project of the Research Council of Norway (grant number UB101292101) for partially supporting the master's studies.

Finally, I would like to thank any family, friends and students who helped and supported me during the studies.

Fahim Masud Ahmed
Bergen, Norway, May 2023

"To live is to suffer, to survive is to find some meaning in the suffering."

Friedrich Nietzsche

Abstract

Over the years, wind turbines have been steadily increasing in size, with newer models boasting larger dimensions. For instance, the diameter of an installed prototype offshore wind turbine in late 2022 was over 200 m, which is significantly larger than in 2010, where the average size was 90 m. This results in new interactions between the wind turbine and the atmosphere in the form of Low-Level Jets (LLJs). The thesis aims to study the effect of a LLJ on the wind-induced response of a 15 MW offshore wind turbine. Engineering tools, i.e. TurbSim and OpenFAST, were used to simulate the turbulence boxes and the load response of a large offshore floating turbine. The results showed that the interaction between the LLJ profiles and the wind turbine response is not trivial, and the development of the loads as the LLJ height increases can't be described by one single pattern. They were however closely related to the aerodynamic loads.

Contents

Chapter 1

Introduction

1.1 Motivation

A tracking report by IEA (2022) stated that the electricity generation from wind energy increased by 17% from 2020 to 2021. Apart from hydro power, wind is the largest source of renewable energy production, and wind energy increased by a record amount in 2021 including all power generation methods. The majority of wind energy production comes from onshore wind turbines, and it dominated the capacity installed in 2021. However, onshore wind power production is a developed technology. Unlike onshore wind, offshore wind is at the start of its era, and the offshore sector is expected to grow in the coming years.

Innovations in wind turbine technology often focus on the development of larger wind turbines to capture more of the wind energy (IEA, 2022). This is due to the fact at wind power is proportional to the square of the rotor radius and to the cube of the wind speed. At a higher altitude, the wind speeds are generally higher. As a consequence, the wind turbine dimensions have increased since the early 2000s (EERE, 2022). This limits the innovations of onshore technology, as wind turbine dimensions are often hindered by environmental policies and public acceptance. In contrast, for offshore applications, these restrictions do not apply (IEA, 2022). Problems with visual and noise impact are reduced depending on the distance from shore, and the transportation of components is not restricted by the road sizes (Breton & Moe, 2009). Additionally, the development of floater technology enables the use of

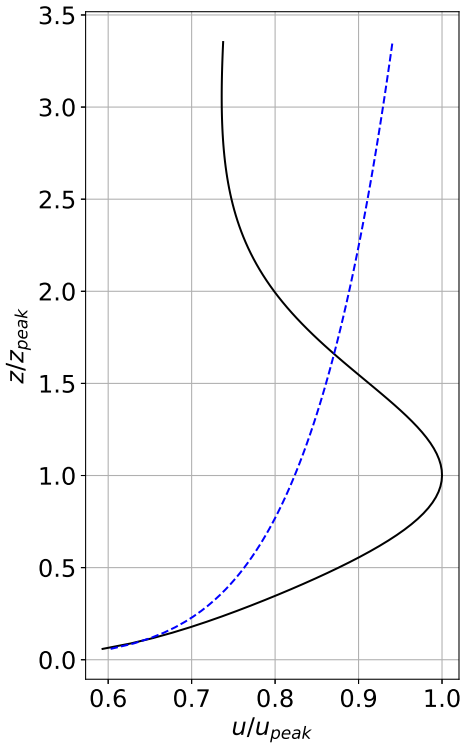

Figure 1.1: Comparison of a LLJ profile (black line) vs a traditional wind profile (dashed blue line). Normalized in terms of LLJ core-speed (x-axis) and LLJ height (y-axis).

deeper waters, where large amounts of potentially suitable areas are unlocked (Archer & Jacobson, 2005). For water depths larger than 50 m, it is impractical with bottom-fixed foundations due to issues with installation, cost and decommissioning (IEA, 2022).

As wind turbines grow in size, the frequency of interactions between Low-Level Jet (LLJ) peaks and wind turbines will increase (Gutierrez et al., 2017). LLJs are air currents with high velocity in the Atmospheric Boundary Layer (ABL) (Stull, 1988). They are characterized by a peak of the wind speed on top of the stable nocturnal inversion layer (Blackadar, 1957). The height and core-speed of the LLJ varies significantly depending on the site.

1.2 Problem Statement

In light of increasing wind turbine sizes, it may be important to assess the differences in structural loading due to varying LLJ heights. Thus, the main research question of this thesis is: *How does the LLJ height affect the structural loading of a large floating wind turbine?* To do this, the thesis will utilize a wind turbine engineering tool, i.e. OpenFAST, capable of applying various physics models. Three-dimensional wind fields will be generated using TurbSim, which is a turbulence generator. Additionally, the thesis will also briefly mention *how the LLJs affect the aerodynamic loads*, since the aerodynamics loads are directly related to the structural loads.

A peak implies regions of positive and negative shear. As wind turbines have been designed the expectation of positive shear, the effects of negative shear have not been thoroughly studied (Gutierrez et al., 2017; Zhang et al., 2019). Furthermore, an assessment of the sensitivity of the atmosphere on wind turbines is critical for improving turbine design and efficiency (IEA, 2022). To the author's knowledge, negative shear is rarely considered in wind turbine design. Thus, the thesis explored how the structural and aerodynamics loads were affected by the LLJ. It is found that the interaction between the LLJs, structural and aerodynamic loads are not trivial.

The rest of the thesis is divided in the following way. Chapter 2 describes background theory. The section will mention aerodynamics, hydrodynamics, structural dynamics and the atmosphere. Chapter 3 describes the design of the research and section 3.2 describes the simulation tools. Chapter 4 presents and discusses the results of the thesis, and section 4.4 outlines the limitations of the thesis. Lastly, chapter 5 presents the final conclusion of the thesis and provides insight into any further work necessary.

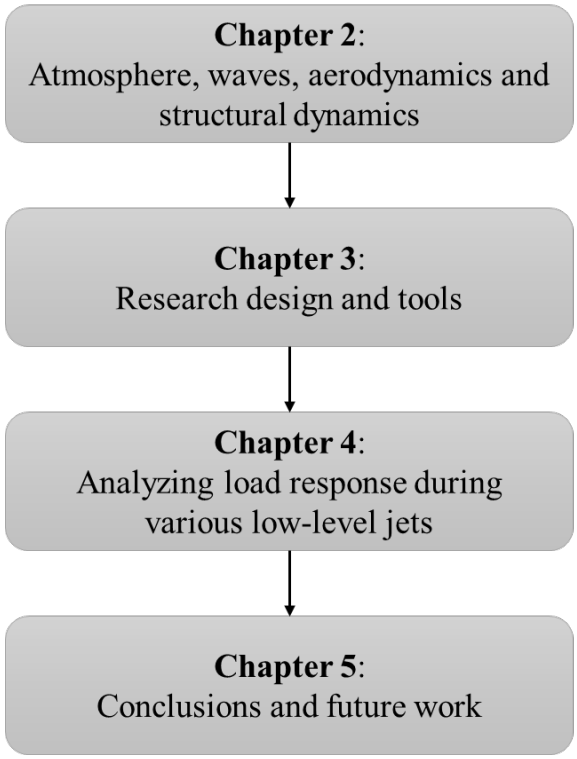

Figure 1.2: Thesis outline.

Chapter 2

Theory

This chapter describes the theoretical background necessary for understanding the dynamics of floating offshore wind turbines. It starts by introducing some previous studies related to the research question.

2.1 Previous studies

A previous study by Gutierrez et al. (2017) considered the effects of negative shear inside the rotor swept area on the turbine's response. In their paper, a quantity which described the amount of negative shear inside the rotor swept area was derived, and then it was gradually modified to develop different LLJ cases. The authors concluded that the presence of negative shear generally lead to lower loading with respect to a traditional wind profile, and recommended to build larger turbines. This result was attributed to the lower value of absolute shear in the negative shear region and the lower magnitude of distributed loads, both leading to lower forces and moments.

Another study by Ahmed & Paskyabi (2023) compared the effects of a LLJ shear on wind turbine loading with a traditional power-law wind profile. In the paper, the LLJ height was at hub height, and the profiles below hub height were kept equal. The authors generally observed a lower wind turbine loading in the presence of a LLJ. However, higher loading during a LLJ was observed for the streamwise and spanwise moments at the tower top.

Zhang et al. (2019) studied the effects of LLJ core-speed on aero-

dynamic loads when the LLJ was located at hub height. The authors established a model for the LLJ wind profile with a user-defined von Karman spectral model. The conclusion of the paper was that the aerodynamic loads increased with LLJ core-speed. The authors attributed this to the increasing wind shear which caused unbalanced aerodynamic loading.

2.2 Wind power

Wind turbines produce energy by converting the kinetic energy of the wind to mechanical energy. The mechanical energy is converted to electrical energy by the generator. The power available in the wind is given by the following equation (Ehrlich, 2013).

$$P_{wind} = \frac{1}{2}\rho A_{rotor} V_{\infty}^{3}, \tag{2.1}$$

where ρ is the air density, A_{rotor} is the rotor swept area and V_{∞} is the free stream velocity of incoming wind. In reality, only a fraction of this energy is extracted by the wind turbine, and the efficiency of the wind turbine is given by the power coefficient C_p. Thus, a general formulation for the extracted power can be expressed as (Ehrlich, 2013):

$$P = P_{wind} C_p. \tag{2.2}$$

The wind behind the turbine would have to stand still to convert all of the energy, and this is not physically possible. Therefore, there exists a limit to the maximum efficiency of a wind turbine, i.e. Betz limit $C_{p,max} = 0.593$ (Betz, 1920).

2.3 Atmospheric Boundary Layer (ABL)

The lower part of the troposphere is affected by the surface friction. This part of the atmosphere is known as the Atmospheric Boundary Layer (ABL). The lowest 10% of the ABL is defined as the Atmospheric Surface Layer (ASL) (Stull, 1988).

2.3.1 Atmospheric Surface Layer (ASL)

The characteristics of turbulence and mean variables in the ASL are relatively simple, albeit important. This is because most engineering problems are related to the ASL characteristics. The characteristics are influenced by both mechanical and thermal forcing, thus, the Monin-Obukhov similarity theory (Monin & Obukhov, 1954) was developed to explain the ASL characteristics. Monin & Obukhov (1954) introduced two scaling parameters, namely the surface friction velocity u_* and the length L, which stays constant through the ASL (Panofsky & Dutton, 1984).

The surface friction velocity u_* is a rewritten form of the surface stress in units of velocity. It depends on the surface shear stress τ_0 and the air density ρ_a (Stull, 1988).

$$u_* = \sqrt{\frac{\tau_0}{\rho_a}} = \left(\overline{u'w'}^2 + \overline{v'w'}^2\right)^{\frac{1}{4}}. \tag{2.3}$$

A physical interpretation of the Monin-Obukhov length L is that it is proportional to the height where buoyancy effects first dominate the mechanical shear production (Stull, 1988). Furthermore, the scaling length L can be used to define a ratio z/L to describe the relationship between buoyancy and shear. The ratio z/L is given by (Kaimal & Finnigan, 1994):

$$\frac{z}{L} = \frac{(g/\overline{\theta})(\overline{w'\theta'})_s}{u_*^3/\kappa z}, \tag{2.4}$$

where $(\overline{w'\theta'})_s$ is the temperature flux in the surface layer, $\overline{\theta}$ is the mean potential temperature, $g = 9.81$ ms^{-2} is the gravitational acceleration and κ is the von Kármán constant, and typically, $\kappa = 0.4$. The aforementioned ratio is defined by $\zeta \equiv \frac{z}{L}$ (Stull, 1988), and the sign of ζ is directly connected to the static stability of the ABL (Kaimal & Finnigan, 1994).

- A negative ζ suggests a statically unstable atmosphere,
- a positive ζ suggests a statically stable atmosphere.

Various atmospheric properties are functions of z/L when normalized by u_* and L, however, in the case of mean wind profiles, this

does not hold. Rather, the (logarithmic) wind profile is derived from integrating $\frac{\partial \overline{u}}{\partial z}$, where the surface roughness z_0 length appears (Panofsky & Dutton, 1984). The roughness length z_0 is the height above the surface where the wind velocity is zero, and it is directly related to the surface elements. After z_0 has been determined, it does not change with temperature or stability conditions (Stull, 1988), although it is affected by changes in the surface (e.g. growth of grass, foliation, lumbering). Above the sea surface, the roughness length is dependent on the sea state and wave conditions. In 1955, Charnock proposed a relationship to calculate the roughness length above the ocean (Charnock, 1955).

$$z_0 = a_c \frac{u_*^2}{g}, \tag{2.5}$$

where a_c is Charnock's constant (Charnock, 1955). It is important to keep in mind that the observed value of a_c varies widely (Wu, 1980).

Theoretically, the surface layer parameters are to be strictly defined by the surface fluxes, however, in practice, the parameters are often calculated with measurements from some convenient height (Kaimal & Finnigan, 1994).

2.3.2 The mean wind speed profile

The mean vertical wind shear in neutral stability can be represented with the logarithmic wind profile (Stull, 1988).

$$u_{Log}(z) = \frac{u_*}{\kappa} ln\left(\frac{z}{z_0}\right), \tag{2.6}$$

where z is the height above the surface. The logarithmic wind profile can also be rewritten with a stability correction to account for different stability conditions (Businger et al., 1971). This equation is derived from applying Monin-Obukhov similarity theory (Stull, 1988).

An alternative to the logarithmic profile is the Power-Law (PL) wind profile, which is an empirical relationship given as (Frost, 1948):

$$u_{PL}(z) = u_{ref}\left(\frac{z}{z_{ref}}\right)^{\alpha}, \tag{2.7}$$

where u_{ref} is a reference velocity at a reference height z_{ref} and α is the shear exponent. α is an empirical constant that describes the stability (Frost, 1948). It is typically set to 0.14 (onshore) or 0.11 (offshore) for neutral atmosphere (Hsu et al., 1994), but it can be adjusted for non-neutral stability conditions. In Newman & Klein (2014), values for the shear exponent for different stability regimes were extrapolated. Generally, the shear exponent increased with increasing stability, which was expected (Petersen et al., 1998).

2.3.3 Turbulence as a random process

Wind velocity fluctuations are three-dimensional and the components are denoted $i = u, v, w$. The components can be separated into a mean part (denoted by an overline) and a fluctuating part (denoted by an apostrophe). This is a common approach used in wind analysis, and it is known as Reynolds decomposition. Furthermore, the assumption of horizontal flow is often made, thus, $\overline{v} = \overline{w} = 0$ (Stull, 1988).

$$u = \overline{u} + u', \tag{2.8}$$

$$v = \overline{v} + v', \tag{2.9}$$

$$w = \overline{w} + w'. \tag{2.10}$$

Turbulence can be visualized as swirls of motion of different sizes. These are called **eddies**, and turbulence consists of eddies of several different sizes. The surface is responsible for most of the turbulence in the ABL. Turbulence can be generated either by mechanical effects (i.e. terrain, hills) or buoyancy effects. The buoyancy effects are due to the sun heating up the surface and causing vertical convection. Turbulent wind fluctuations are suppressed by a statically stable atmosphere or through dissipation into heat (Stull, 1988).

Turbulence is defined as a random process, which means that it is a collection of random variables that are functions of time. In this thesis, one assumes homogeneous, stationary, Gaussian and ergodic turbulence. The first two assumptions imply that the statistical properties do not change in space and time, respectively. The Gaussian turbulence assumption means that the turbulent fluctuations follow a Gaussian distribution. Lastly, the ergodic assumption means that the

statistical properties of turbulence can be derived from a single time series assuming that is it long enough (Cheynet & Jakobsen, 2022).

Information about the turbulence characteristics in the ABL is often needed in wind turbine design, bridge design, weather forecast, etc. However, it is difficult to create a large, three-dimensional picture of the atmosphere. An alternative approach stating that turbulence can be considered **frozen** was suggested by Taylor in 1938. In this approach, the wind velocities are measured at one location over a period of time and converted to spatial measurements (Stull, 1988). This is known as Taylor's hypothesis, and the general expression of the equation is shown below (Tong, 1996).

$$s'(\mathbf{x},t) = s(\mathbf{x} - \mathbf{U}t), \tag{2.11}$$

where s' is a variable at a fixed point $\mathbf{x}$, s is the spatial signal of the same variable and $\mathbf{U}$ is the mean convection velocity (Tong, 1996). Physically, this means that the characteristics of turbulence might be considered constant while it passes through a sensor. It is important to remember that turbulence is never truly frozen and this simplification is useful in cases where the time evolution of turbulence is slow (Stull, 1988).

In wind energy, two parameters are widely used to quantify the turbulence levels in the ABL: Turbulence Intensity (TI) for the u-component and Turbulence Kinetic Energy (TKE). The former is defined as the ratio between the standard deviation of the wind component and the mean wind velocity in x-direction (Stull, 1988). The TI is a function of height, and should generally decrease with height (European Committee for Standardization, 1991).

$$TI_i = \frac{\sigma_i}{\overline{u}}. \tag{2.12}$$

The latter is a measure of the kinetic energy in turbulence, and is related to the velocity variances u', v', w' (Stull, 1988). It is widely used in Computational Fluid Dynamics (CFD). The equation for the TKE is often given in terms of per unit mass (Stull, 1988).

$$\frac{TKE}{m} = \frac{1}{2}(\overline{u'^2} + \overline{v'^2} + \overline{w'^2}). \tag{2.13}$$

In wind engineering, the coherence and the wind spectrum are important quantities for studying wind-induced loading on the turbines. To define them, the thesis will first define spectral density. Take two stationary data sets, $M(t)$ and $N(t)$. The correlation function shows the relationship between them. It is termed cross-correlation function if the data sets represent different quantities. If the data sets represent the same quantity (i. e. $M(t) = N(t)$), which is a special case, the correlation function is termed the autocorrelation function. By taking the Fourier transform of the correlation function, the spectral density function is derived. This aforementioned naming convention also applies for the spectral density function, where the functions are called Cross-Spectral Density (CSD) and Power Spectral Density (PSD), respectively. The general equations for the spectral density functions, S_{MN} and S_{MM} respectively, are given by (Bendat & Piersol, 1980):

$$S_{MN}(\omega) = \int_{-\infty}^{+\infty} R_{MN}(\tau) e^{-i\omega t} d\omega, \tag{2.14}$$

$$S_{MM}(\omega) = \int_{-\infty}^{+\infty} R_{MM}(\tau) e^{-i\omega t} d\omega, \tag{2.15}$$

where R_{MM} is the autocorrelation function, τ is a time lag, ω is the angular frequency and R_{MN} is the cross-correlation function. The spectral densities are often estimated using algorithms based on the Fast Fourier Transform (FFT) such as the Welch's algorithm. Furthermore, the correlation functions themselves are usually calculated with the FFT.

The wind spectrum is the spectral density of the wind fluctuations, and gives the power of the wind as a function of the frequency (Cheynet & Jakobsen, 2022). It is often estimated using spectral models, particularly an empirical formulation described by Kaimal et al. (1972) known

as the Kaimal spectral model. The Kaimal spectral model is given as:

$$\frac{fS_u(f)}{u_*^2} = \frac{105 f_r}{(1+33 f_r)^{\frac{5}{3}}}, \tag{2.16}$$

$$\frac{fS_v(f)}{u_*^2} = \frac{17 f_r}{(1+9.5 f_r)^{\frac{5}{3}}}, \tag{2.17}$$

$$\frac{fS_w(f)}{u_*^2} = \frac{2 f_r}{\left(1+5.3 (f_r)^{\frac{5}{3}}\right)}, \tag{2.18}$$

$$\frac{fS_{uw}(f)}{u_*^2} = -\frac{14 f_r}{(1+9.6 f_r)^{2.4}}, \tag{2.19}$$

where $S_u(f)$, $S_v(f)$, $S_w(f)$ and $S_{uw}(f)$ are the wind spectra and $f_r = fz/\overline{u}$ is a non-dimensional frequency (Kaimal et al., 1972).

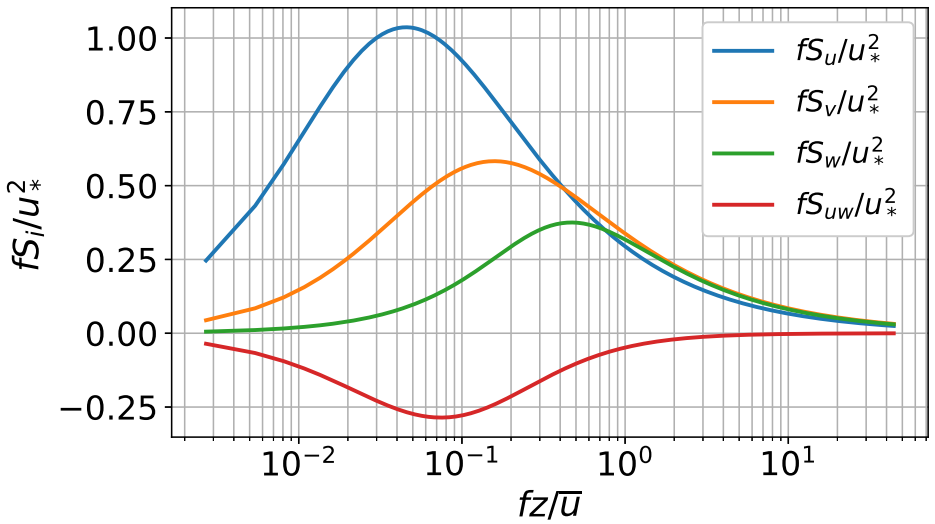

Figure 2.1: An example of the Kaimal spectral model.

The coherence, which is the normalized 2-point CSD of the velocity fluctuations, is used to study the correlation of turbulence between two points in the frequency domain (Ropelewski et al., 1973). The root of the coherence is called the root-coherence. The root-coherence can be split into a real part and an imaginary part. The real part is called the co-coherence and the imaginary part is called the quad-coherence (Watson, 1975). In wind engineering, the quad-coherence is often ignored, and

the root-coherence is approximated with the co-coherence (Cheynet et al., 2017).

$$Coh_i(y_1, y_2, f) = \frac{Re\{S_i(y_1, y_2, f)\}}{\sqrt{S_i(y_1, f) S_i(y_2, f)}}, \tag{2.20}$$

where $S_i(y_1, y_2, f)$ is the CSD of the i-th component between two points y_1 and y_2, $S_i(y_1, f)$ is the PSD for the i-th component at location y_1 and $S_i(y_2, f)$ is the PSD for the i-th component at location y_2. Note that Eq. (2.20) is only applicable for the lateral separation.

In 1961, Davenport showed that the vertical co-coherence could be estimated using an exponential function. This model is known as the Davenport coherence model, and it is given by the following function (Davenport, 1961).

$$\gamma_i(y_1, y_2, f) = exp\left(-c_1^i \frac{fr}{\overline{u_m}} \right), \tag{2.21}$$

where c_1^i is a decay coefficient for wind components $i = u, v, w$, r is the distance between the two points y_1 and y_2, and $\overline{u_m}$ is the mean wind velocity between the two points. In 1970, Pielke & Panofsky (1970) discussed the extension of Eq. (2.21) to other directions, and remarked that the data supported the extension of the Davenport coherence model to the lateral and longitudinal directions.

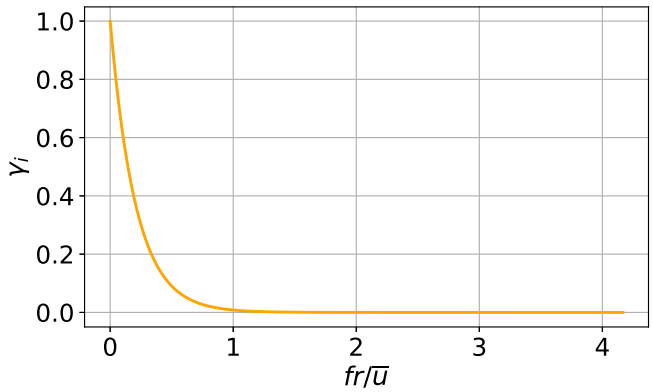

Figure 2.2: An example of the Davenport coherence model.

2.3.4 Stability

The local lapse rate Γ in Eq. (2.22) describes the vertical temperature gradient, and defines the static stability. The wind velocity does not affect the static stability. The ABL is typically defined as statically unstable if $\Gamma > 0$, neutral if $\Gamma = 0$ and stable if $\Gamma < 0$. Physically, the static stability can be interpreted in the following way (Stull, 1988):

1. $\Gamma > 0$ (unstable): an air parcel perturbed upwards (downwards) will continue to move away from its origin due to the surrounding air having higher (lower) density,

2. $\Gamma = 0$ (neutral): a vertically perturbed air parcel will remain at its new location due to the surrounding air having the same density,

3. $\Gamma < 0$ (stable): an air parcel perturbed upwards (downwards) will move back towards its origin due to the surrounding air having lower (higher) density.

$$\Gamma = -\frac{\partial T}{\partial z}. \tag{2.22}$$

Vertical convection takes place when the warmer air is beneath the colder air due to density differences. This promotes turbulent fluctuations, and this occurs in statically unstable atmosphere. On the contrary, the colder air underlies the warmer air in a statically stable atmosphere. This results in less convective mixing. The latter usually occurs at night, and compared to the former description, the latter has an inverted temperature gradient. Thus, this layer (at night) is often called the nocturnal inversion layer (Stull, 1988).

The lapse rate may not be enough to classify neutral stability. Neutral stability is defined by two things: the adiabatic lapse rate and the lack of convection. Convection can still exist even when $\Gamma = 0$. Thus, non-local variables such as the heat flux (or direct measurements) are necessary to identify neutral stability (Stull, 1988).

A way to quantify the stability of the atmosphere is with the Richardson number, which is the relationship between buoyancy and shear effects. There are several forms of the equation for the Richardson number. The form most often used is known as the gradient Richardson

number Ri_g (Kaimal & Finnigan, 1994).

$$Ri_g = \frac{\frac{g}{\overline{\theta}}\frac{\partial \overline{\theta}}{\partial z}}{\left(\frac{\partial \overline{u}}{\partial z}\right)^2}, \tag{2.23}$$

The type of flow (turbulent or laminar) depends on the sign and value of Ri_g. The transition between turbulent and laminar flow is governed by the critical Richardson number $R_{crit} = 0.25$, and this value was by both theory and observations (Panofsky & Dutton, 1984).

The stability parameters ζ and Ri are similar, but the usefulness of ζ is boosted compared to Ri. This is a result of the Monin-Obukhov similarity theory (see section 2.3.1), as ζ can be considered constant through the surface layer (Kaimal & Finnigan, 1994).

2.3.5 Low-level jet formation

LLJs have been observed both above land and sea (Wagner et al., 2019). However, the formation mechanism may be different depending on the location (Pichugina et al., 2017; Wagner et al., 2019). LLJs occur commonly above the Great Plains, and the formation is usually linked to Inertial Oscillations (IOs) (Blackadar, 1957; Pichugina et al., 2017). Baroclinic effects, which are the effects of temperature and pressure on the density, are often mentioned as the cause for LLJ occurrences in coastal areas (Jiang et al., 2010; Pichugina et al., 2017; Guest et al., 2018). Furthermore, winds crossing the land-sea border might experience a decoupling from the surface. This happens since the ocean surface is less rough compared to the land, thus, the winds crossing experience an acceleration resulting in a LLJ (Wagner et al., 2019). In the IO mechanism (Blackadar, 1957), the wind above the surface is disconnected and it experiences less friction (Stull, 1988; Gutierrez et al., 2014; Paskyabi et al., 2022). The pressure-gradient forces accelerate the wind to near-geostrophic speeds (Stull, 1988). Additionally, an IO is induced due to a disparity between the pressure-gradient forces and the Coriolis force (Stull, 1988; Gutierrez et al., 2014; Paskyabi et al., 2022). Thus, the wind speed fluctuates about the geostrophic wind (Stull, 1988). The period of oscillation, called the ***inertial period***, is given by $T = \frac{2\pi}{f_C}$, where f_C is the Coriolis force (Stull, 1988). This usually

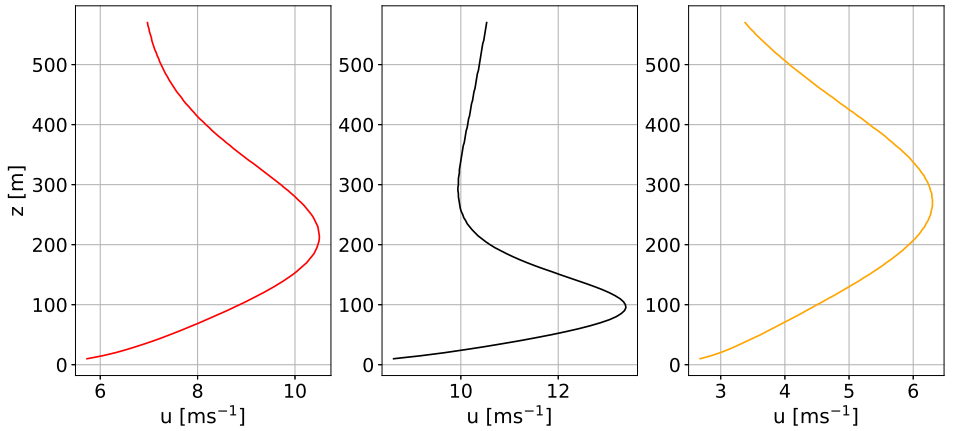

Figure 2.3: Examples of different LLJ wind profiles with different core-speeds and heights.

happens at sunset, when daytime convection is reduced (Blackadar, 1957; Gutierrez et al., 2014), and a nocturnal inversion starts to form (Blackadar, 1957). Later at night, the daytime subgeostrophic wind is accelerated to supergeostrophic speeds (Blackadar, 1957; Stull, 1988; Paskyabi et al., 2022).

In the baroclinicity mechanism, a horizontal temperature gradient causes a sloped isobaric surface. According to the ***thermal wind*** relationship (see Eqs. (2.24) and (2.25)) (Stull, 1988), the geostrophic wind V_g will decrease with height z if the temperature T decreases in the x-direction (Stull, 1988; Paskyabi et al., 2022). In the case where the wind is geostrophic everywhere except near the surface, where the wind speeds are reduced due to frictional drag, a LLJ can occur. This can happen either at day or night, however, it is more likely to occur at night due to the large amounts of convective mixing at daytime. The horizontal temperature gradient can be caused by several mechanisms such as sloping terrain, cold fronts or land-sea differential heating (Stull, 1988). If the horizontal temperature gradient is caused by a sloping terrain, the direction (and LLJ core-speed) might oscillate with the

diurnal cycle (Holton, 1967).

$$\frac{\partial U_g}{\partial z} = -\frac{g}{f_C T}\frac{\partial T}{\partial y}, \tag{2.24}$$

$$\frac{\partial V_g}{\partial z} = +\frac{g}{f_C T}\frac{\partial T}{\partial x}. \tag{2.25}$$

The formation of LLJ might happen due to a combination of effects (Stull, 1988; Wagner et al., 2019; Paskyabi et al., 2022), which makes studying formation mechanisms challenging (Wagner et al., 2019). Above the Southern North Sea, the LLJ formation is attributed to both IOs and baroclinic effects (Wagner et al., 2019). Furthermore, the IO LLJ is dependent on geostrophic winds, which itself is dependent on baroclinic effects (Paskyabi et al., 2022).

2.4 Waves

The generation of waves starts when pressure perturbations in the atmosphere disturbs the ocean surface. This causes small capillary waves which diminishes when the wind reduces due to surface tension. In the event where the wind does not reduce, and affects the surface over a longer period, waves big enough can occur where gravity acts as a restoring force. These are commonly known as surface gravity waves, and are of most importance in regards to marine structures (Massel, 1996).

Generally, one would assume that the mean surface elevation is of most interest, however, observers tend to notice the larger waves in the ocean, making this definition rarely used. Rather, definition based on a visual approach is preferred, namely the significant wave height H_s (Holthuijsen, 2007). The significant wave height was originally introduced by Sverdrup & Munk (1947) as the average wave height of the third highest waves, however, it is now commonly defined by the standard deviation of the wave record (Massel, 1996).

$$H_s = 4\sigma_\eta, \tag{2.26}$$

The significant wave period T_p is another important wave characteristic, which was defined as the average of the third highest wave

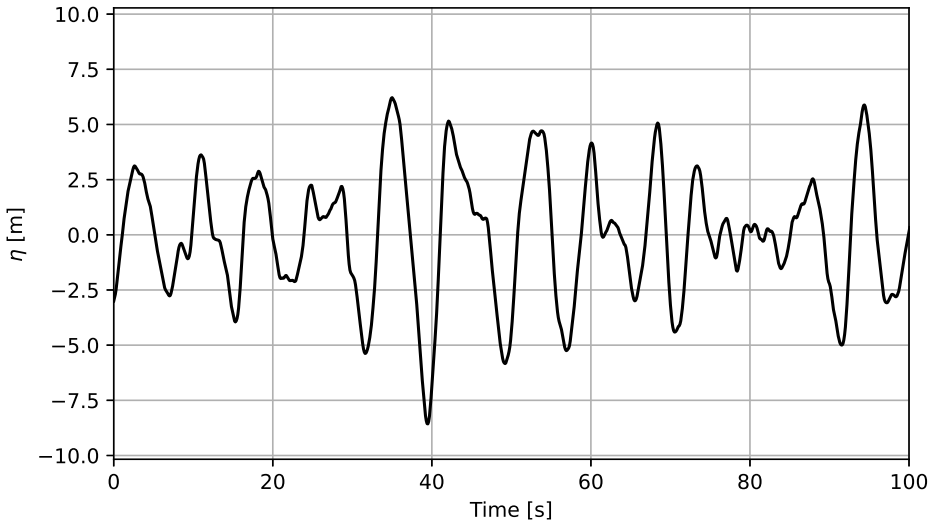

Figure 2.4: Example of a wave elevation time series. Based on JONSWAP spectrum with $H_s = 10$ m and $T_p = 8$ s.

periods. However, the significant wave period can be estimated with the spectrum. Based on observational data, the significant wave period is nearly equal to the peak period (Holthuijsen, 2007).

2.4.1 Governing equations for fluid flow

The governing equations for fluid flows are the continuity equation (conservation of mass) and the Navier-Stokes momentum equation (conservation of momentum). For an incompressible fluid, they are respectively (Benitz et al., 2015; Kundu et al., 2016).

$$\nabla \cdot \mathbf{u} = 0, \tag{2.27}$$

$$\rho\left(\frac{\partial \mathbf{u}}{\partial t} + \mathbf{u} \cdot \nabla \mathbf{u}\right) = -\nabla p + \rho \mathbf{g} + \mu \nabla^2 \mathbf{u}, \tag{2.28}$$

where $\mathbf{u}$ is the velocity vector, p is the pressure, $\mathbf{g}$ is the gravity vector, μ is the viscosity, ρ is the fluid density and t is time. Assuming irrotationality and constant-density, the momentum equation can be simplified (Kundu et al., 2016).

$$\rho\left(\frac{\partial \mathbf{u}}{\partial t} + \mathbf{u} \cdot \nabla \mathbf{u}\right) = -\nabla p. \tag{2.29}$$

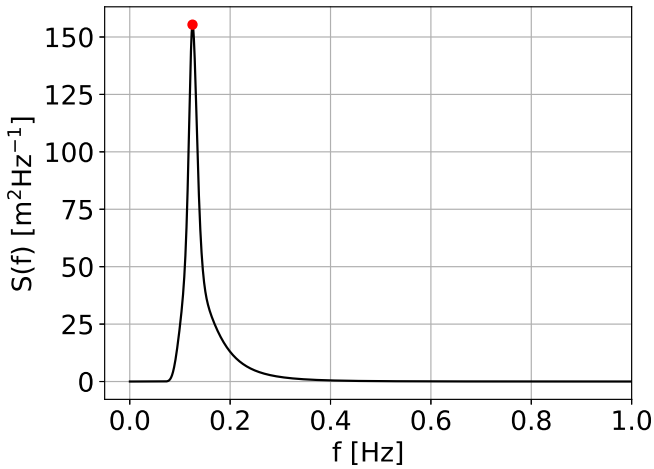

Figure 2.5: The JONSWAP spectrum of which Fig. 2.4 is based on. Red dot shows the peak spectral period ($\approx$ significant wave period) T_p.

This is the form of the momentum equation used for ideal flows. It is applicable for inviscid, irrotational and homogeneous flows. The ideal flow theory is widely used in aero- and hydrodynamics (Kundu et al., 2016).

It is important to note that the incompressibility assumption often means constant-density, however, in reality the flow may still have baroclinic density variations. Therefore, the constant-density assumption needs to be explicitly made for the application of Eq. (2.29) (Kundu et al., 2016).

In potential flow theory, the fluid is considered inviscid. The velocity vector field can be defined as the gradient of a scalar function, called the velocity potential ϕ. The velocity potential can be applied in any irrotational flow, and such flows are often called potential flows (Benitz et al., 2015; Kundu et al., 2016).

$$\mathbf{u} = \nabla\phi \tag{2.30}$$

2.4.2 Linear wave theory

The surface elevation η is given by (Kundu et al., 2016):

$$\eta(x,t) = a\cos(kx - \omega t), \tag{2.31}$$

where a is the amplitude, $k = \frac{2\pi}{\lambda}$ is the wave number, λ is the wavelength, $\omega = \frac{2\pi}{T}$ is the angular frequency and T is the wave period. The phase speed c, which is the travel speed of a wave crest, is given as $c = \frac{\omega}{k}$. The wave period is given by $T = \frac{2\pi}{kc}$ (Kundu et al., 2016).

Linear wave theory is concerned with waves with small amplitudes and small slopes, i.e. $a/\lambda << 1$ and $a/H << 1$, respectively. H is the depth of the liquid layer, i.e the ocean. Ideal flow (incompressible, irrotational, inviscid) is assumed, and the velocity potential is applied to the continuity equation. This leads to the continuity equation to be rewritten as the Laplace equation (Kundu et al., 2016).

$$\nabla^2\phi = \frac{\partial^2\phi}{\partial x^2} + \frac{\partial^2\phi}{\partial z^2} = 0, \tag{2.32}$$

where the velocity components are defined as $u = \frac{\partial\phi}{\partial x}$ and $\frac{\partial\phi}{\partial z}$. To solve the above Laplace equation, three boundary conditions are needed (Kundu et al., 2016):

1. The normal velocity of the fluid is zero at the bottom of the liquid layer.

2. The velocity of the fluid-particle normal to the surface and on the surface is equal to the velocity of the surface normal to itself. This ensures that the interfaces remains defined, and the fluid-particles at the surface do not move away from the interface.

3. The pressure right below the surface is equal to the ambient pressure. This means that the surface is considered as a free surface where the stresses are neglected.

By choosing the initial condition $\eta(x, t = 0) = a\cos(xt)$ and using the first two boundary conditions the following solution for the velocity potential is derived (Kundu et al., 2016).

$$\phi = \frac{a\omega}{k}\frac{\cosh(k(z+H))}{\sinh(kH)}\sin(kx - \omega t), \tag{2.33}$$

which results the following equations after substituting Eq. (2.33) into

the definitions for the velocity components (Kundu et al., 2016).

$$u = a\omega \frac{\cosh(k(z+H))}{\sinh(kH)} \cos(kx - \omega t), \tag{2.34}$$

$$w = a\omega \frac{\sinh(k(z+H))}{\sinh(kH)} \sin(kx - \omega t). \tag{2.35}$$

By using the last boundary condition, a relationship between ω and k can be derived. This is known as the dispersion relation (Kundu et al., 2016).

$$\omega = \sqrt{gk \tanh(kH)}. \tag{2.36}$$

The dispersion relation can be applied to the phase speed to derive the following equation (Kundu et al., 2016).

$$c = \frac{\omega}{k} = \sqrt{\frac{g}{k} \tanh(kH)}. \tag{2.37}$$

The dispersion relation is a fundamental concept in linear wave theory as it shows that waves are dispersive because the speed depends on the wave number. Physically, this means that waves with longer wavelength will travel faster than waves with shorter wavelength (Kundu et al., 2016).

2.4.3 Morison's equation

The Morison's equation is a widely used approach to model the hydrodynamic loads on an offshore structure, specifically surface-piercing structures. It is an empirically based equation valid for slender bodies, and it consists of two terms: drag and inertia, respectively (Morison et al., 1950).

$$F_{Morison} = \frac{1}{2}\rho C_{drag} A_p |U_f| U_f + \rho C_m V_{obj} \frac{dU_f}{dt}, \tag{2.38}$$

where C_{drag} is the drag coefficient, A_p is the projected area of the structure, U_f is the fluid velocity, C_m is the inertia coefficient and V_{obj} is the fluid displacement volume.

There are a few limitations in the Morison's equation. It doesn't account for fluctuating lift forces, it cannot model the inline forces accurately, ignores hysteresis and it uses a long-wavelength assumption.

The latter is used to simplify the diffraction modelling, which is how the wave scatters when hitting an impermeable object. However, even with the aforementioned limitations, the model works well for load prediction (Benitz et al., 2015).

2.4.4 JONSWAP spectrum

Spectral representation is used to accurately represent a variety of sea states. A wave spectrum represents the energy in the total wave field as a function of frequency. The most common spectral model is the JONSWAP spectrum. The JONSWAP spectrum is an empirical model based on measurements in the North Sea (Hasselmann et al., 1973).

2.5 Aerodynamics

This section describes the 1-D momentum theory and the blade-element momentum theory. These are important in wind engineering, particularly the latter, since the aerodynamic loads are of interest. Furthermore, the theories are often used in engineering tools to model the aerodynamics.

2.5.1 1-D momentum theory

The 1-D momentum theory is a simple method to describe the aerodynamics of a wind turbine. The rotor is modelled as a permeable disc with a constant wind load across the rotor. Two important factors are to be introduced before describing this method: the axial induction factor a and the tangential induction factor a'. The induction factors describe how the free wind velocity changes as it reaches the rotor plane. The axial wind is reduced, thus, the actual wind velocity at the rotor can be written as $u_{rotor} = (1-u)V_{\infty}$. On the contrary, the tangential wind is increased, and can be written as $u_{tangent} = (1+a')\omega r_d$, where r_d is the distance from the rotational axis (Letcher, 2017).

In the 1-D momentum theory, one assumes that the wind cannot cross the streamlines at the rotor tip. In addition, the assumption of no external losses is made. Thus, the power can be described by the mass flow rate at the rotor and the velocity deficit. Furthermore, the pressure

drop caused by the rotor can be described by applying Bernoulli's equation separately for the upstream and downstream streamline (Letcher, 2017).

By deriving a thrust equation with the axial momentum theory and applying the above definitions, the power coefficient C_P and the thrust coefficient C_T can be derived in terms of the axial induction factor a (Letcher, 2017).

$$C_P = 4a(1-a)^2, \tag{2.39}$$

$$C_T = 4a(1-a). \tag{2.40}$$

Keep in mind that Eq. (2.40) is only valid for low values for the axial induction factor, typically $a \geq 0.3$ (Letcher, 2017).

2.5.2 Blade-Element Momentum Theory (BEMT)

A limiting factor of the 1-D momentum theory is that it doesn't consider the geometry of the blades. A way to overcome this issue is by combining the 1-D momentum theory with the Blade Element Theory (BET). In BET, the aerodynamic loads are considered at each section of the blade, and the wind inflow is considered as the vector sum of the inflow velocity and the angular velocity of the rotor. The combination of both theories lead to the Blade-Element Momentum Theory (BEMT) (Letcher, 2017). In BEMT, the rotor is again considered as a disc, however, the disc is divided into annular rings. It is assumed that each annular ring is independent and that there are an infinite amount of blades (Letcher, 2017). To calculate the normal force F_n (thrust) and tangential force F_t (torque) at each blade section, three quantities are required: the angle between the relative incoming wind and the rotor plane ϕ, the lift force l and the drag force d. These are given as (Letcher, 2017):

$$\tan\phi = \frac{(1-a)V_\infty}{(1+a')\omega r_d}, \tag{2.41}$$

$$l = \frac{1}{2}\rho V_{rel}^2 c C_l, \tag{2.42}$$

$$d = \frac{1}{2}\rho V_{rel}^2 c C_d, \tag{2.43}$$

where c is the chord line, V_{rel} is the relative velocity, r_d is the distance of the section from the axis of rotation, C_l is the lift coefficient and

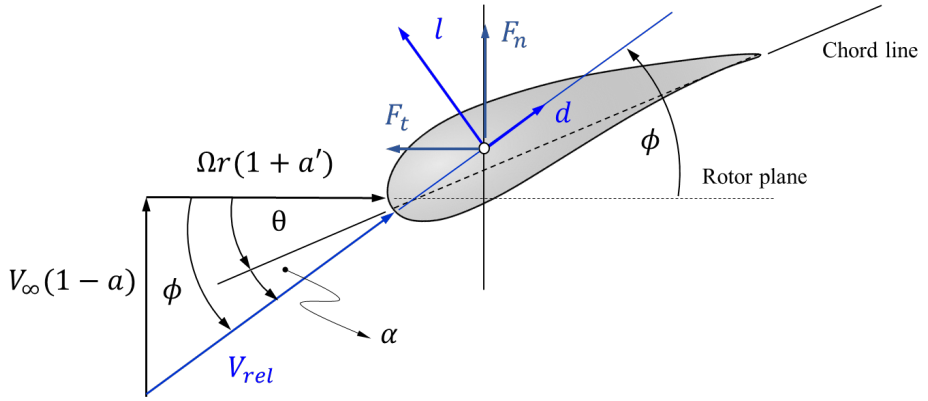

Figure 2.6: Aerodynamic forces and associated angles on an airfoil. Copyright ® 2023 by Dr. Bruno A. Roccia, Geophysical Institute. BOW, UiB. All rights reserved.

C_d is the drag coefficient. The coefficients are provided by a look-up table for the airfoil and are functions of the angle of attack. Then, the aerodynamic forces can be defined (Letcher, 2017):

$$F_n = l\cos\phi + d\sin\phi, \tag{2.44}$$

$$F_t = l\sin\phi - d\cos\phi. \tag{2.45}$$

The aerodynamic forces can be applied further to define the thrust coefficient C_T and the tangential induction factor a' (Letcher, 2017).

$$C_T = 4aF_P(1-a), \tag{2.46}$$

$$a' = \frac{1}{\frac{4F_P\sin\phi\cos\phi}{\sigma C_t} - 1}. \tag{2.47}$$

where F_P is the Prandtl tip loss factor, $\sigma = \frac{Bc}{2\pi r_d}$ is the solidity and $C_t = C_l\sin\phi - C_d\cos\phi$ is the tangential coefficient. The Prandtl tip loss factor is a correction applied to account for the infinite blade assumption made at the beginning. It is important to remember that Eq. (2.46) is not valid for large values for the axial induction factor, typically $a \geq 0.3$ (Letcher, 2017).

2.6 Structural dynamics

Structural dynamics is how a structure behaves when affected by dynamic loading. For a floating wind turbine, the dynamics have to be modelled for both the turbine and the floating platform. Thus, two equations of motions are of importance: one for the floating platform and one for the body.

2.6.1 IEA reference wind turbine

The wind turbine model used in this thesis was the IEA 15 MW Reference Wind Turbine (RWT) (Gaertner et al., 2020) with a semi-submersible floating platform as the supporting structure (Allen et al., 2020). The RWT was developed by IEA, whilst the modelling of the floating platform was a collaborative effort between NREL and the University of Maine (UMaine). The controller consists of a variable speed and collective pitch system, and the drivetrain is a direct-drive system (Gaertner et al., 2020).

2.6.2 Equation of motion for a floating platform

The motions of a floating platform is governed by the following (linearized) equation of motion (Nielsen, 2021):

$$(\boldsymbol{M}+\boldsymbol{A})\ddot{\boldsymbol{\eta}}+(\boldsymbol{B_v}+\boldsymbol{B_r})\dot{\boldsymbol{\eta}}+(\boldsymbol{C_m}+\boldsymbol{C_h})\boldsymbol{\eta}=\boldsymbol{F_{wa}}+\boldsymbol{F_{wi}}+\boldsymbol{F_{cu}}+\boldsymbol{F_{wt}}, \tag{2.48}$$

where $\boldsymbol{M}$ is the dry mass matrix, $\boldsymbol{A}$ is the added mass matrix, $\boldsymbol{B_v}$ is the damping matrix, $\boldsymbol{B_r}$ is the added damping matrix, $\boldsymbol{C_m}$ is the stiffness matrix, $\boldsymbol{C_h}$ is the added stiffness matrix, the four forces are the excitation forces due to wave, wind, current and the wind turbine itself, and η is the motion vector (Nielsen, 2021).

The first term of the equation consists of the dry mass matrix and the added mass matrix. The dry mass matrix includes the mass and the moment of inertia of the platform. The moment of inertia is a measure of the body's resistance to change in angular momentum. The added mass matrix includes the moment of inertia due to the movement of fluid surrounding the body (Nielsen, 2021).

Rated power	15 MW
Hub height	150 m
Rotor diameter	120 m
Cut-in, rated, cut-out wind speed	3 ms^{-1}, 10.59 ms^{-1}, 25 ms^{-1}
Minimum, maximum rotor speed	5 rpm, 7.56 rpm
Maximum tip speed	95 ms^{-1}
Tip speed ratio	9
Draft	20 m
Total system mass	20093 t
Mooring system	Three-line chain catenary
1st tower FA bending mode	0.493 Hz
1st tower SS bending mode	0.483 Hz
Surge ω_n	0.007 Hz
Sway ω_n	0.007 Hz
Heave ω_n	0.049 Hz
Roll ω_n	0.036 Hz
Pitch ω_n	0.036 Hz
Yaw ω_n	0.011 Hz

Table 2.1: Main properties of the 15 MW RWT. FA denotes fore-aft direction, SS denotes side-to-side direction and ω_n is the natural frequency (Gaertner et al., 2020; Allen et al., 2020).

The second term consists of the damping and added damping. Damping is connected to the pressure distribution over the body due to flow separation. This means that the drag of the body is directly related to the geometry of the body and the flow conditions. The added damping is the contribution of the radiated waves from the floating body, and it is a linear contribution to the total damping matrix. Physically, this means that a body submerged deeper (shallower) generates less (more) waves, which causes the radiation damping to be larger (lesser) (Nielsen, 2021).

The third term consists of the stiffness and added stiffness. The stiffness matrix is the contribution from the mooring lines to the restor-

ing forces. The added stiffness accounts for the restoring forces due to the surrounding fluid and buoyancy effects (Nielsen, 2021).

2.6.3 Kane's equation of motion

Kane's Equation of Motion (KEoM), which is a rewritten form of Newton's second law of motion, has been widely used to study multi-body dynamics. In wind engineering, this is useful since the wind turbine structure consists of several bodies connected at the joints. Therefore, KEoM can be used to simulate the structural dynamics of a wind turbine. The general formulation is given as (Roithmayr & Hodges, 2016):

$$F_j + F_j^* = 0, \tag{2.49}$$

where F_j are the generalized active forces, F_j^* are the generalized inertia forces and j are the degrees of freedom. The active forces are forces that are directly affecting the system either by contact and/or at distance (i.e aerodynamics, hydrodynamics, etc.). The inertia forces depend on the mass of the system (i.e. nacelle mass, tower mass, etc.) (Roithmayr & Hodges, 2016).

2.6.4 Damage equivalent load

Comparisons of structural loading between incident wind fields is important in the wind industry to evaluate the differences. However, if using a standard statistical measure (e.g. mean, median), the variations in the loading are lost. Even by using the standard deviation of the time series, only the amplitude is considered, and the number of oscillations is lost (Nybø et al., 2021). A way to overcome this issue is to use the Damage Equivalent Load (DEL) (Frandsen & Christensen, 1994), which accounts for both the amplitude of the time series and the number of oscillations by using the Rainflow cycle-counting algorithm (Matsuishi & Endo, 1968).

$$DEL = \left(\frac{\sum_i (R_i^m n_i)}{N_{eq}} \right)^{\frac{1}{m}}, \tag{2.50}$$

where R_i is the load range for i-th cycle, n_i is the number of cycles for i-th cycle, m is the Wöhler exponent and N_{eq} is a number of

equivalent cycles (Frandsen & Christensen, 1994). The Wöhler exponent is dependant on the material. For steel and composites, the Wöhler exponent is 3 and 10, respectively (IEC, 2015).

Chapter 3

Methods

This chapter describes the case studies, the load responses and their definitions, the procedure for obtaining the results, and the modelling tools used in this thesis.

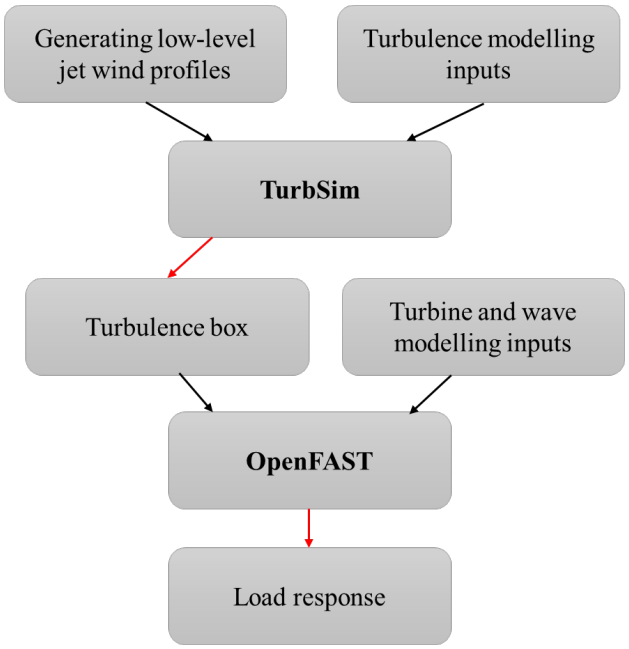

Figure 3.1: Modelling flowchart of this thesis. Black (red) arrow denotes input (output).

3.1 Research design

The thesis studied 15 different LLJ cases. Three different LLJ core-speeds were chosen based on the power curve of a 15 MW wind turbine (Gaertner et al., 2020): below rated, at rated and above rated wind speed. This way, the thesis gathered information of how the turbine reacted regardless of the amount of response from the control system. At each LLJ core-speed, five LLJ heights were selected.

Three locations for the load response were chosen: tower base, tower top and blade root. For each location, both streamwise and spanwise loads were studied. These were selected based on parameters used in previous studies (e.g. Gutierrez et al. (2017); Ahmed & Paskyabi (2023)), and based on where the author expected the largest responses. The interface between the substructure (yellow) and tower (orange) is the tower base, the interface between the tower (orange) and nacelle (grey) is the tower top and the interface between the hub (blue) and blade (green) is the blade root (shown in Fig. 3.2).

Specifically, the 12 load responses were: tower base streamwise shear force, tower base spanwise shear force, tower base spanwise moment, tower base streamwise moment, tower top streamwise shear force, tower top spanwise shear force, tower top spanwise moment, tower top streamwise moment, blade root out-of-plane shear force, blade root in-plane shear force, blade root in-plane moment and blade root out-of-plane moment.

The thesis also looked at the aerodynamic loads along the blades since the aerodynamics are closely related to the structural loading. This was mainly the thrust (normal to the rotor plane) and torque (tangential to the rotor plane). In addition, the lift (normal to the chord) and drag (tangential to the chord) were also briefly mentioned. For further elaboration on the aerodynamic forces, see section 2.5.2.

To better understand the streamwise structural loads on a wind turbine, I simplified the wind turbine (in Fig. 3.2) as a vertical cantilever beam with a mass on top (in Fig. 3.3). When a force is applied on the mass on top (i.e. rotor thrust), it will induce a streamwise shear force and a bending moment at the interfaces. Since much of the energy in a LLJ wind profile is concentrated at the LLJ core, it was somewhat expected to find a correlation between the LLJ height, the corresponding

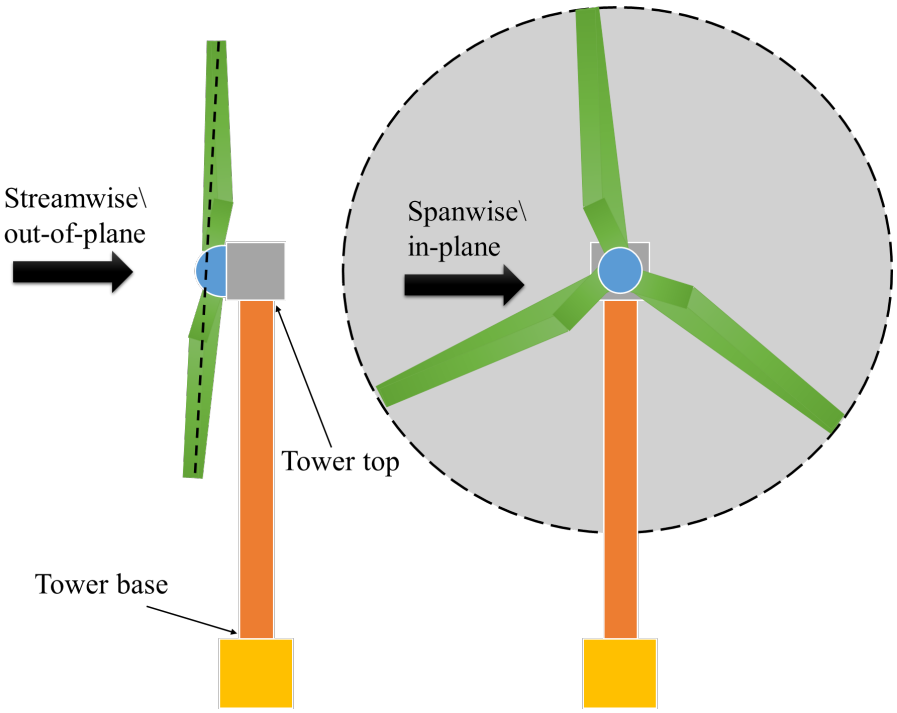

Figure 3.2: Definitions of the streamwise, spanwise, out-of-plane and in-plane directions. Dashed lines indicate the rotor plane.

summed thrust force and the pattern of how the DEL developed. In addition, the mean hub velocity also likely plays a role in governing the loads due to the mode shapes. As the LLJ height increases to the hub height, the mean wind velocity at the hub increases. When the LLJ moves upwards from the hub height, the mean wind velocity at the hub height decreases.

3.1.1 Constructing low-level jet profiles

The LLJ wind profiles in this thesis were developed according to methodology described in Zhang et al. (2019). The authors established a model for the LLJ inflow based on the theory of plane wall jet. The expression was developed by combining the power-law equation with a free jet term. Additionally, a shape function was multiplied with the free jet term to satisfy the no-slip condition. The final expression is shown

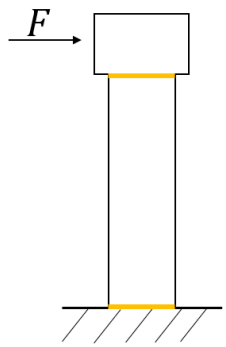

Figure 3.3: Simplified model of a wind turbine. F is an applied force and the yellow lines show the interfaces. Upper (lower) yellow line denotes the tower top (base).

below (Zhang et al., 2019).

$$v_{LLJ}(z) = \left\{ v_{ref} + v_m \left[1 - \tanh^2 \left(C_s \frac{z - z_s}{z_s} \right) \right] \right\} \left(\frac{z}{z_{ref}} \right)^{\alpha}, \qquad (3.1)$$

where z is the height, v_{ref} is a reference velocity, v_m is the jet velocity, C_s is a shape parameter, z_s is the jet height, z_{ref} is the reference height and α is the shear exponent (Zhang et al., 2019).

Based on Eq. (3.1), a function was developed to generate a group of LLJs. By choosing a reference LLJ core-speed, the function can generate a group of random LLJs by varying the LLJ height. In this case, the function was run three times with three different LLJ core-speeds: below rated (6.8 ms^{-1}), at rated (10.59 ms^{-1}) and above rated (17.8 ms^{-1}). For each case, LLJs with five different heights were picked from the group: 70 m, 110 m, 150 m, 190 m and 230 m, corresponding to $(2/3)R$ below hub height, $(1/3)R$ below hub height, at hub height, $(1/3)R$ above hub height and $(2/3)R$ above hub height, where $R = 120$ m is the rotor radius. The wind profiles are shown in Fig. 4.1.

3.1.2 Generating turbulence boxes

The wind profiles mentioned in section 3.1.1 were provided as inputs to TurbSim for the generation of the turbulence boxes. For each wind profile, 10 seeds were simulated to reduce the randomness in synthetic

turbulence. The IEC recommends 6 seeds, however, a larger value was picked to study uncertainties due to random errors. The simulation time was set to 720 seconds, and the first 120 seconds were removed to eliminate the model spin-up time. This was selected to follow the IEC recommendation of 600 s of simulated data. The wind spectrum was generated internally by TurbSim with the IEC Kaimal spectral model, which is a slightly modified version of the original Kaimal spectral model. When utilizing this model in TurbSim, the Richardson number is automatically set to 0. The wind direction was set to 0°, meaning that the wind inflow was always perpendicular to the rotor plane. Turbulence intensity was set constant as 5% across the simulations. This value was based on a paper by Schepers et al. (2021), where the authors observed a similar value for the TI at 150 m (i.e. hub height) during a LLJ event. Coherence was modelled with the Davenport model, and only the decay coefficients were provided to TurbSim. The decay coefficients were calculated with the following model by Cheynet et al. (2018).

$$c_1^u = 11 + 1.8\exp(4.5\zeta), \tag{3.2}$$

$$c_1^v = 7.1 + 3.4\exp(6.8\zeta), \tag{3.3}$$

$$c_1^w = 3.5 + 0.7\exp(2.5\zeta), \tag{3.4}$$

where c_1^u is the decay coefficient for the u-component, c_1^v is the decay coefficient for the v-component, c_1^w is the decay coefficient for the w-component and ζ is the stability parameter. The aforementioned model was deemed accurate for $-2 < \zeta < 0.2$ by the authors. Since LLJs mainly occur in stable atmospheric conditions, when the Monin-Obukhov length L and ζ are positive, the thesis assumes $\zeta = 0.2$. The model for the decay coefficients are really for vertical separations, however, there is a lack of detailed database of the lateral coherence under stable stratification (Putri et al., 2022).

The surface roughness length z_0 is generally between 0.001 and 0.0001 above the ocean surface depending on the sea state (Panofsky & Dutton, 1984). However, the inputs in TurbSim are rounded to three decimals. Thus, the author decided to keep z_0 constant at 0.001 across the simulations.

The grid dimensions were 350 m by 350 m with 36 nodes in each direction. The time step was selected as 0.05 s, which corresponds to 20 Hz.

Input parameter	Selection
Spectral model	IEC Kaimal
IEC standard	$61400-3$
Turbulence intensity, TI	5%
Decay coeff. c_1^u	15.427
Decay coeff. c_1^v	20.347
Decay coeff. c_1^w	4.654
Surface roughness length z_0	0.001

Table 3.1: A summary of inputs used in TurbSim.

3.1.3 Calculating structural loading

The turbulence boxes were provided as inputs to OpenFAST, which calculated the load response of the wind turbine. The Kane's Equation of Motion (KEoM) was solved using Adams-Bashforth-Moulton 4th order predictor corrector method to calculate the loads. The integration time step was 0.010 s, corresponding to 100 Hz, and this value was chosen to keep the solution stable. From previous experience, a larger time step sometimes caused errors in the software. The environmental conditions used in OpenFAST are shown in Table 3.2.

The waves were generated internally with the HydroDyn module. The wave elevation time series was based on the JONSWAP spectrum with the significant wave height H_s and the significant wave period T_p

Environmental parameter	Value
Gravity	9.81 ms^{-2}
Air density	1.225 kgm^{-3}
Water density	1025 kgm^{-3}
Kinematic viscosity of air	1.464×10^{-5} $\mathrm{m}^2\mathrm{s}^{-1}$
Speed of sound in air	335 ms^{-1}
Water depth	200 m
Offset between still-water and mean sea level	0 m

Table 3.2: Environmental conditions used in OpenFAST.

as inputs. Both parameters were parameterized in terms of the mean wind speed at 10 m (U_{10}) and calculated individually for each wind profile. The parametrization is shown below (Carter, 1982):

$$H_s = 0.0248U_{10}^2, \tag{3.5}$$

$$T_p = 0.729U_{10}. \tag{3.6}$$

An alternative approach would be to use a joint probability distribution function. However, this would require access to measurement data for both wind and wave. For the sake of simplicity, the aforementioned approach was taken.

3.2 Modelling tools

This section describes the wind engineering tools utilized in this thesis, i.e. TurbSim and OpenFAST.

3.2.1 TurbSim v2.00

TurbSim is a random turbulence generator based on statistical models and it generates fluctuations for three velocity components in a two-directional plane. The velocity time series is generated by performing an inverse Fourier transform to the user-specified spectral model. Alternately, the spectral model/time series can be generated externally and used as inputs in the software (Jonkman, 2014).

3.2.2 OpenFAST v3.4.1

OpenFAST is a multi-fidelity engineering tool. The main driver module combines an array of sub-modules to calculate the aero-servo-hydro-elastic dynamics of a wind turbine. The relevant sub-modules are as follows: AeroDyn, ElastoDyn, HydroDyn, ServoDyn and InflowWind (NREL, 2023).

AeroDyn calculates the aerodynamic loads on both the tower and blades for a wind turbine. It is coupled to the OpenFAST driver, however, it can also be used as a standalone software. The modelling of the structure is based on the actuator line model, where the tower and

blades are modelled as lines with nodes. The local forces at each node are calculated based the Blade-Element Momentum Theory (BEMT) (Jonkman et al., 2017).

The ElastoDyn module is responsible for the wind turbine model and the structural dynamics. The load and motion quantities for the wind turbine are calculated based on KEoM. The equations are solved numerically with an Ordinary Differential Equation (ODE) solver (Jonkman & Jonkman, 2016).

The HydroDyn module is responsible for the sea state and hydrodynamic loads. The wave conditions can be modelled as either regular or irregular waves, either internally or externally. The waves are generated with a combination of first (linear) and second-order wave theory (alternatively, second order wave theory can be turned off), and the wave spectrum is based on JONSWAP. The hydrodynamics loads are calculated with a combination of potential flow theory and Morison's equation (Jonkman, 2009).

ServoDyn is responsible for the control system of the wind turbine. This includes the blade pitch control, generator control, generator properties (i.e. efficiency, start-up, shut-down), torque control, braking controls and nacelle-yaw controls. Additionally, tuned mass and liquid dampers can be defined (Jonkman & Buhl, 2005).

The InflowWind module is responsible for the wind inflow, and the inflow can be generated either internally or externally. Internally, only the generation of steady inflow is possible. Externally, a wide range of file formats and inflow types are supported (e.g. binary TurbSim full-field, bladed-style full-field, etc.). Taylor's frozen turbulence hypothesis is used to translate the flow to three dimensions (Platt et al., 2016).

Chapter 4

Results and Discussion

This chapter presents the results of different case studies. 15 case studies were performed, and they consisted of five LLJ heights for three LLJ core-speeds (shown in Fig. 4.1). As mentioned in chapter 3, the shear forces and bending moments were analyzed for three response locations: tower base, tower top and blade root in streamwise and spanwise directions.

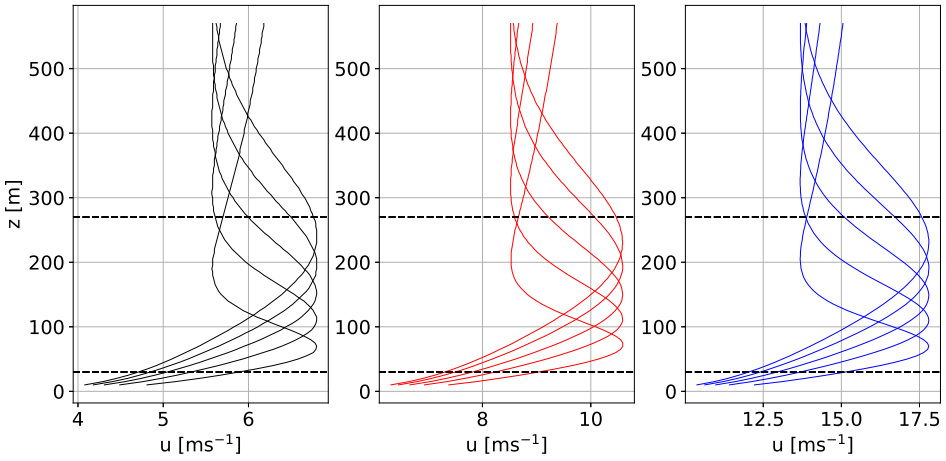

Figure 4.1: LLJ with varying heights for three different cases: below rated wind speed (left), at rated wind speed (middle), and above rated wind speed (right). LLJ core-speed for each respective case is 6.8 ms^{-1}, 10.59 ms^{-1} and 17.8 ms^{-1}. The dashed horizontal lines show the rotor swept area.

4.1 Aerodynamic loads

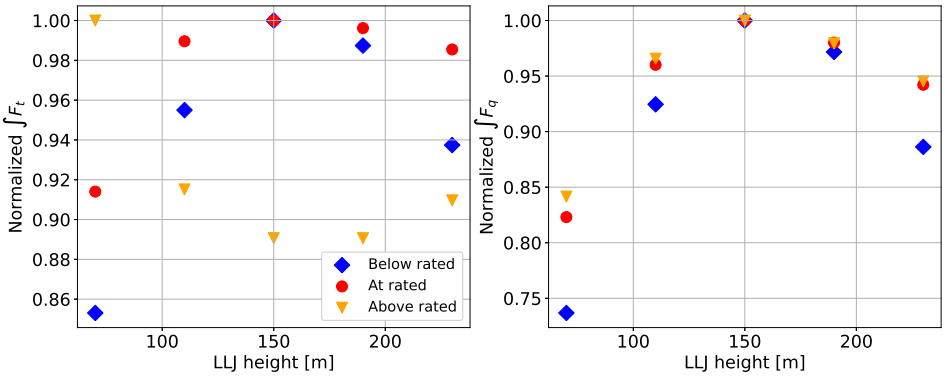

Figure 4.2: Normalized sum of the aerodynamic loads for each LLJ core-speed at each LLJ height.

Figure 4.2 reveals that the sum of the distributed aerodynamic loads along the blade span are similar for all LLJ heights, except for the lowest LLJ. This may be explained by the narrow LLJ peak when the peak is close to the surface. Otherwise, the LLJ peaks have similar "peakedness".

The distributed thrust and torque forces when the LLJ core-speed is below and at rated wind speed were roughly alike in pattern (see Figs. 4.3a to 4.3d). However, this changed when the LLJ core-speed was above rated wind speed (see Figs. 4.3e and 4.3f). This was likely caused by the large amounts of blade pitching provided by the control system (see Fig. 4.5), since the nacelle was detecting large wind velocities. I also noticed that the slope in the mean distributed aerodynamic forces when the LLJ was at hub height was generally the steepest regardless of core-speed. This was possibly caused by the imbalanced loads due to half the rotor experiencing positive wind shear and half of the rotor experiencing negative wind shear.

From Fig. 4.2, I also observed that the pattern for the total thrust force changed when the LLJ core-speed was above rated wind speed. Generally, both the total thrust and total torque force are the largest when the LLJ height was at hub height, likely explained by the mean hub velocity. However, the largest value for the total thrust force when

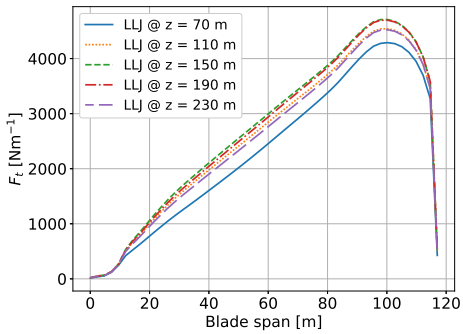

(a) Local F_t for below rated LLJ core-speed.

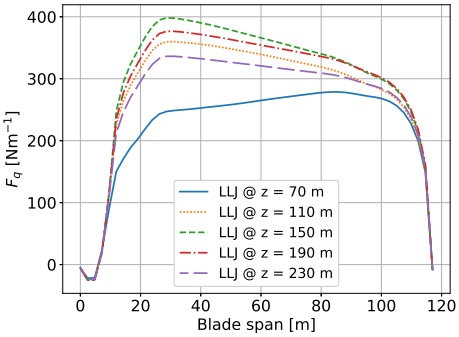

(b) Local F_q for below rated LLJ core-speed.

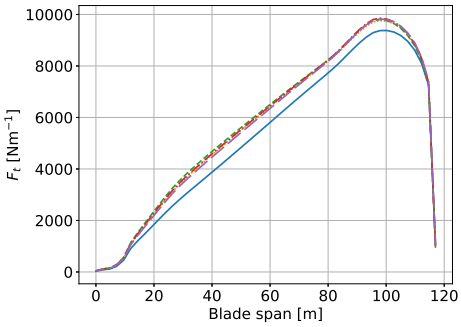

(c) Local F_t for rated LLJ core-speed.

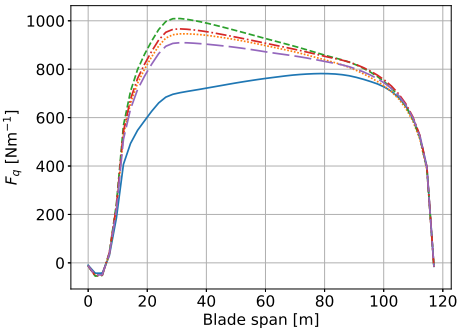

(d) Local F_q for rated LLJ core-speed.

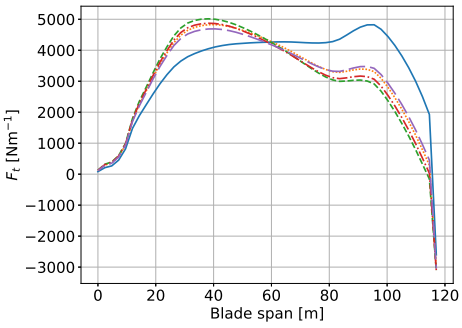

(e) Local F_t for above rated LLJ core-speed.

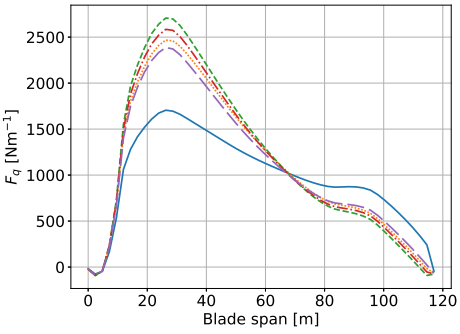

(f) Local F_q for above rated LLJ core-speed.

Figure 4.3: Local mean aerodynamic loads (thrust F_t and torque F_q) along the blade span.

the LLJ core-speed was above rated wind speed occurred when the LLJ was closest to the surface. This was likely due to the blade pitching.

Results from Fig. 4.2 show that the mean hub velocity and the natural blade twist likely played a larger role for the aerodynamic thrust force when the LLJ core-speed was at or under rated wind speed. However, the shape of the LLJ profile likely had a larger role when the LLJ core-speed was above rated wind speed and the control system was in play. Additionally, when the pitch control was active, the height of the LLJ likely played a larger role.

The wind profile with a LLJ at 70 m had a narrow peak which directly impacted the blades. This results in the sum of the time-averaged distribution of normal forces along the blade span to have a high value (see Fig. 4.2). As the LLJ peak travels towards the hub height, the sum decreases. Further, when the LLJ peak moves upwards above the hub height, the sum of the thrust forces increases again due to the LLJ impacting the blades more directly. Although, in this case, I did not observe a perfectly symmetrical behaviour of thrust force. This is likely due to the LLJ peak being narrower for the LLJs closer to the surface.

The height of the LLJ also had an effect on how much the aerodynamic loads varied at the blades nodes (see Fig. 4.4). Generally, the largest standard deviation of the local aerodynamic forces at the blade nodes were observed when the LLJ was closest to the surface. This was likely caused by the large gradients in the vertical wind shear present in the wind profile. Additionally, this interaction seemed to be enhanced when the LLJ core-speed was at rated wind speed. This may be explained due to the fact that the LLJ core-speed was at the very peak of the thrust curve.

The lowest variations in the aerodynamic loads were observed when the LLJ was at hub height. Since half of the rotor is experiencing positive shear, and half the rotor is experiencing negative shear, the LLJ is likely providing some stabilizing effects during a full rotation. Although, a definite answer is hard to provide due to the asymmetric nature. Generally, the further the LLJ peak was from the hub height, the larger aerodynamic variations at the blade nodes were observed (see Fig. 4.4).

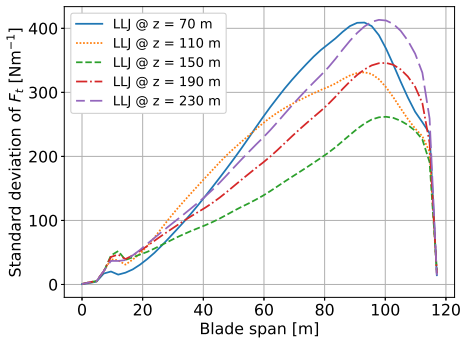

(a) Local F_t for below rated LLJ core-speed.

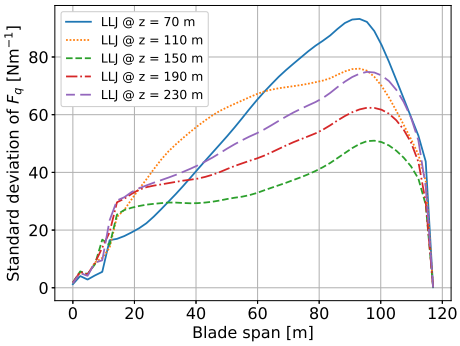

(b) Local F_q for below rated LLJ core-speed.

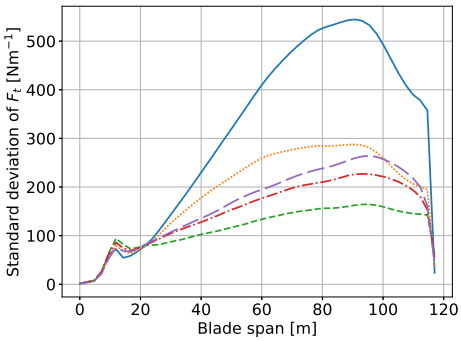

(c) Local F_t for rated LLJ core-speed.

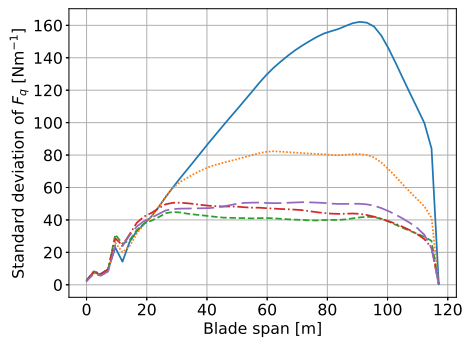

(d) Local F_q for rated LLJ core-speed.

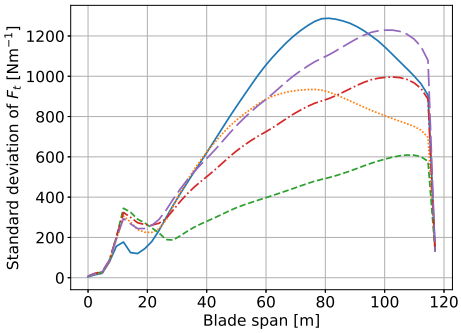

(e) Local F_t for above rated LLJ core-speed.

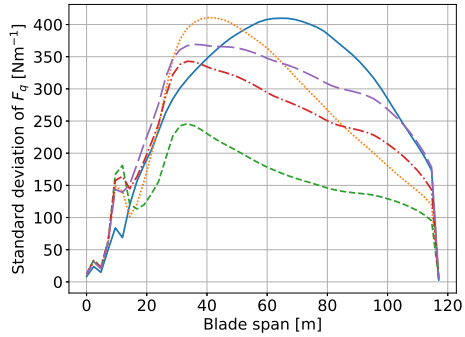

(f) Local F_q for above rated LLJ core-speed.

Figure 4.4: Standard deviation for the local aerodynamic loads (thrust F_t and torque F_q) along the blade span.

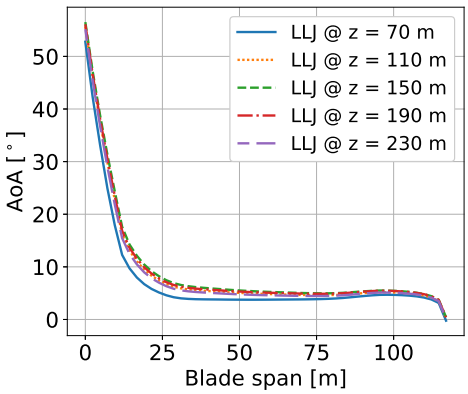

(a) For below rated LLJ core-speed.

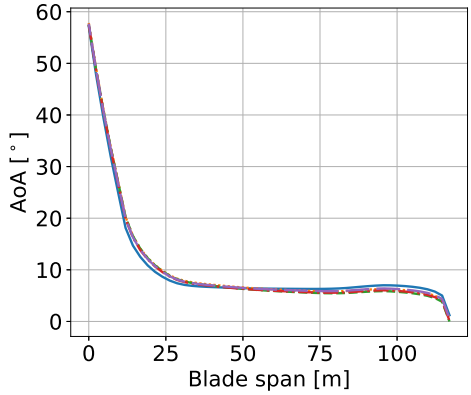

(b) For rated LLJ core-speed.

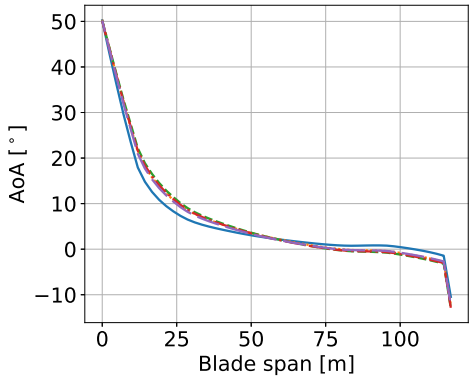

(c) For above rated LLJ core-speed.

Figure 4.5: Local Angle of Attack (AoA) along the blade span.

4.2 Tower loads

This section presents the results for the tower loads corresponding to the different cases. It is divided into four parts. The first two parts (i.e. sections 4.2.1 and 4.2.2) merely present the results. In the last two parts (i.e. sections 4.2.3 and 4.2.4), the results are discussed further and an interpretation is provided. This is done for the sake of brevity.

4.2.1 Tower base loads

This sub-section describes the results found from the case studies for the tower base streamwise and spanwise loads. I divided the section into three segments: below rated, at rated and above rated.

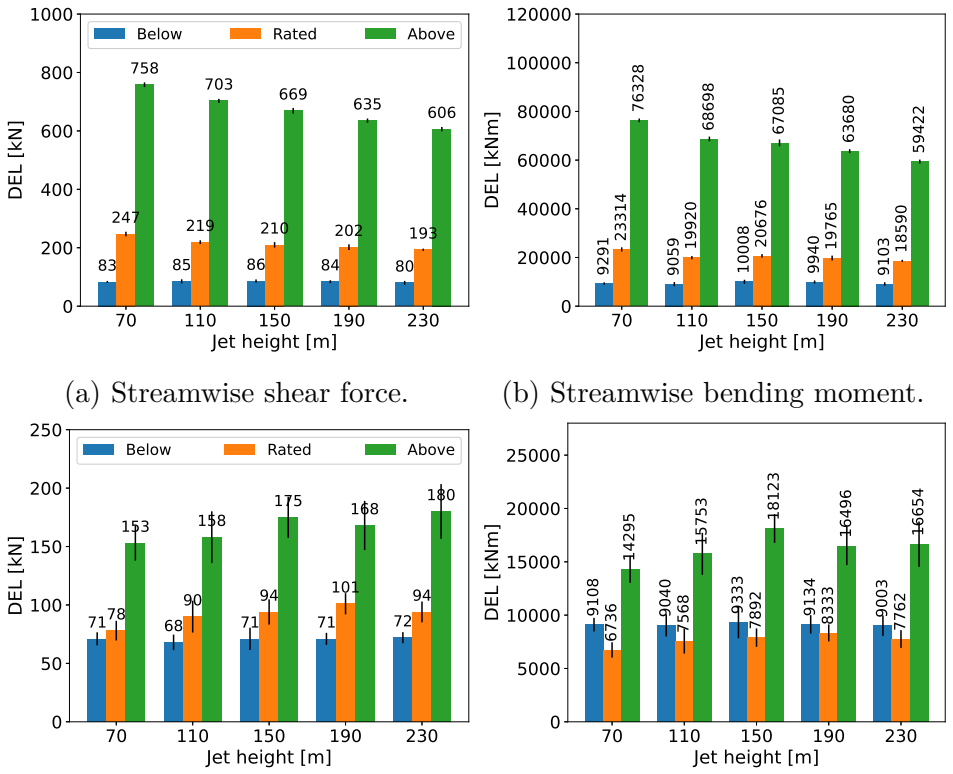

(a) Streamwise shear force.

(b) Streamwise bending moment.

(c) Spanwise shear force.

(d) Spanwise bending moment.

Figure 4.6: Tower base spanwise loads. Error bars show 1 standard deviation.

Below rated:

The tower base streamwise shear force in Fig. 4.6a increased by approx. 4% when the LLJ height moved from 70 m to 150 m. Afterwards, it decreased by approx. 7% when the LLJ height moved from 150 m to 230 m. Although, the absolute value of the differences were small, and might be considered unimportant. Figure 4.6b shows a non-linear trend in DEL for the tower base streamwise bending moment. The DEL decreased and then increased when the LLJ height moved from 70 m to 110 m and 110 m to 150 m, respectively. Then, I observed a decreasing trend when the LLJ height moved upwards from the hub height. However, the change in DEL from LLJ height 150 m to 190 m was $< 1\%$.

The tower base spanwise shear force in Fig. 4.6c was roughly equal for all LLJ heights. I observed an approx. 4% decrease in DEL when the LLJ height moved from 70 m to 110 m, but the DEL went back to its initial value when the LLJ height moved to 150 m. Accounting for the standard deviation across simulations and the absolute value of the differences, I considered this parameter unaffected by LLJ height at this core-speed. This also roughly applies for the tower base spanwise bending moment in Fig. 4.6d, which showed approx. 2% increase when the LLJ height moved from 70 m to 150 m, and approx. 4% decrease when the LLJ height moved from 150 m to 230 m. A slight decrease in DEL was observed when the LLJ height was at 110 m, resulting in a non-linear pattern. However, accounting for the relatively large standard deviation across simulations, I considered this parameter lightly affected by the LLJ height at this core-speed.

At rated:

Figure 4.6a shows a decreasing pattern for the tower base streamwise shear force. The DEL decreased by about 22% when the LLJ height moved from the highest to the lowest position. Although, the largest decrease of approx. 11% was observed when the LLJ height moved from 70 m to 110 m. Then, the DEL declined by approx. 12% till the end. On the contrary, the tower base streamwise bending moment showed a non-linear pattern in Fig. 4.6b. I observed a decrease when the LLJ height moved to 110 m, then an increase when the LLJ height moved

to 150 m. Thereafter, for the last two LLJs, the DEL decreased, taking its lowest value when the LLJ height was at 230 m. The highest values occurred when the LLJ was closest to the surface.

For the tower base spanwise shear force in Fig. 4.6c, I observed a step-wise increase in the DEL when the LLJ height moved from 70 m to 190 m. The total increase was by approx. 29%. Thereafter, the value decreased by about 7% for the last step (from LLJ height 190 m to 230 m). The same pattern was also noticed in the tower base spanwise bending moment (see Fig. 4.6d), with values of approx. 24% and 7%, respectively.

Above rated:

I noticed a decreasing trend for the tower base streamwise shear force in Fig. 4.6c. The same pattern was also observed for the tower base streamwise bending moment in Fig. 4.6b. A decrease of approx. 20% and 22% in DEL was observed when the LLJ height moved from the lowest to the highest, respectively.

The tower base spanwise shear force shows an increasing, albeit non-linear trend in Fig. 4.6c. The DEL increased with the LLJ height until hub height. Then, it decreased when the LLJ height was at 190 m. Lastly, it increased to its highest value when the LLJ moved to 230 m. However, the standard deviation between the simulations was relatively large, thus, it might be difficult to detect the actual trend. It may also be necessary perform more cases to form a pattern. The tower base spanwise bending moment showed a similar pattern in Fig. 4.6d, but the highest DEL occurred when the LLJ was at hub height. Additionally, the increase in DEL when the jet height moved from 190 m to 230 m was $< 1\%$.

4.2.2 Tower top loads

The tower top streamwise and spanwise loads are described in this sub-section. The sub-section is divided into three segments for each LLJ core-speed: below rated, at rated and above rated.

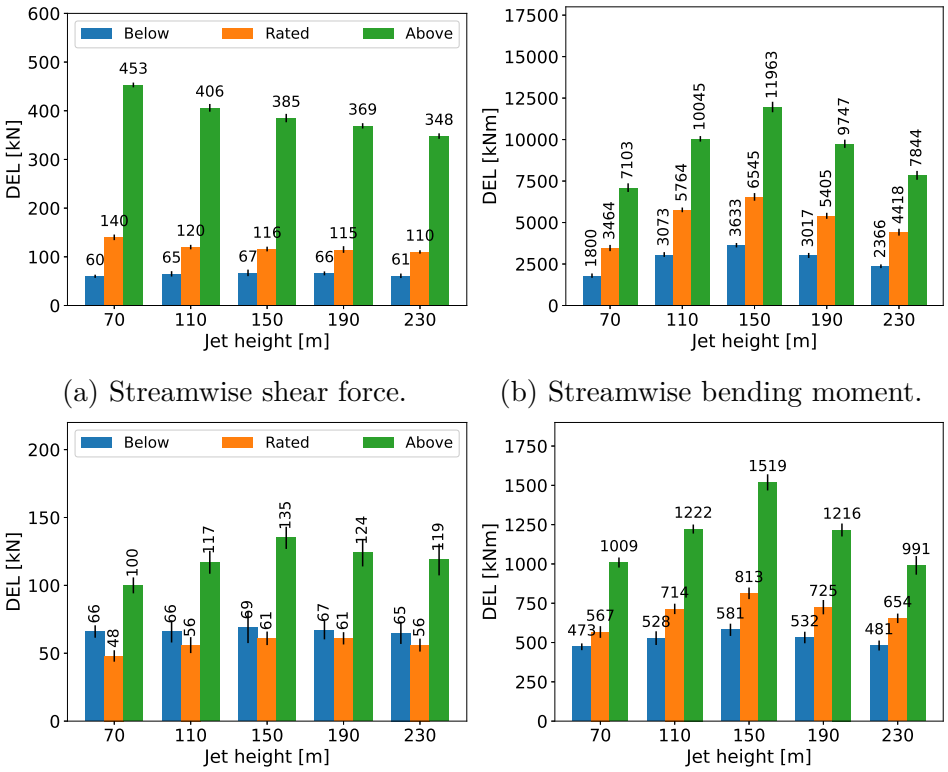

(a) Streamwise shear force.

(b) Streamwise bending moment.

(c) Spanwise shear force.

(d) Spanwise bending moment.

Figure 4.7: Tower top spanwise loads. Error bars show 1 standard deviation.

Below rated:

Figure 4.7a shows that the DEL for tower top streamwise shear force is essentially unchanged when the LLJ is close to hub height, i.e. LLJ height moves from 110 m to 190 m. At the ends (LLJ height 70 m and 230 m), I observed that the DEL is slightly decreased compared to when the LLJ was close to the hub. Although, the absolute value of the difference is small. The tower top streamwise bending moment in Fig. 4.7b shows a similar pattern as the streamwise shear force. However, a more distinct pattern is observed. The DEL increases with LLJ height until hub height. Thereafter, the DEL decreases as the LLJ height increases. The total differences in DEL are 102% and 35%, respectively.

The tower top spanwise shear force (see Fig. 4.7c) remains mainly unchanged across LLJ heights at this core-speed. The values for DEL varied between 65 kN and 69 kN, and I considered this parameter unaffected by the LLJ height at this core-speed. From Fig. 4.7d I observed the same pattern for the spanwise bending moment as the streamwise bending moment (i.e. increasing DEL until hub height, decreasing DEL after hub height). The changes in DEL were approx. 23% and 17%, respectively.

From the LLJ at hub height and upwards, the decrease in the DELs as the LLJ height increases is likely partly related to the absolute values of the positive and negative shear. Essentially, the DELs decreased as the absolute value of both shears decreased. This coincides with Ahmed & Paskyabi (2023), where the authors observed this and briefly mentioned this relationship.

At rated:

Figure 4.7a shows a decreasing pattern for the tower top streamwise shear force. The total decrease of DEL from the highest to the lowest LLJ was approx. 21%. However, the DEL decreased by approx. 14% when the LLJ height increased from 70 m to 110 m. For the tower top streamwise bending moment (Fig. 4.7b), I observed an increasing pattern in the DEL when the LLJ height moved from 70 m 150 m, and a decreasing pattern in the DEL when the LLJ height moved from 150 m to 230 m. The change in DEL was approx. 89% and 32%, respectively.

The DEL for the tower top spanwise shear force (Fig. 4.7c) increased step-wise when the LLJ height moved from 70 m to 150 m. The largest difference occurred when the LLJ height moved from 70 m to 110 m. For the increase in LLJ height from 150 m to 190 m, the DEL remained unchanged. Lastly, from 190 m to 230 m, the DEL decreased slightly. Apart from the first step (i.e. 70 m to 110 m), the values for DEL were similar, especially considering the standard deviation for variations between simulations. For the spanwise tower top bending moment shown in Fig. 4.7d, the DEL increased with the LLJ height until the LLJ was at hub height. Then, the DEL decreased step-wise for the last two LLJ heights. The increase and decrease in DEL were approx. 43% and 20%, respectively.

As mentioned in the last section, the progression of the DELs when the LLJ height moved from 150 m to 230 m is likely related to the absolute values of the positive and negative shear.

Above rated:

Figure 4.7a shows a decreasing trend for the tower top streamwise shear force. The DEL decreased by about 23% from the highest to the lowest DEL. Similar to previous observations, I again observed the largest change in DEL when the LLJ height moved from 70 m to 110 m. The streamwise bending moment at the tower top showed a different trend in Fig. 4.7b. The DEL increased with the LLJ height until hub height, thereafter, it decreased. From the lowest LLJ to the LLJ at hub height, the DEL increased by about 68%. From the LLJ at hub height to the highest LLJ, the DEL decreased by about 34%.

The tower top spanwise shear force showed an increase in DEL until hub height, thereafter it decreased (see Fig. 4.7c). From the lowest LLJ to the LLJ at hub height, the DEL increased by 35%. From the LLJ at hub height to the highest LLJ, the DEL decreased by about 12%. The same pattern was observed for the tower top spanwise bending moment (see Fig. 4.7d). The differences in DEL were approx. 51% and 35%, respectively.

Similar to the two prior cases, the pattern in the DELs caused by the increasing LLJ height (150 m and above) is likely related to the vertical shear. For the sake of brevity, see previous cases.

4.2.3 Further discussion about streamwise tower loads

For the below rated LLJ core-speed, the correlations mentioned in section 3.1 (i.e. a relationship between LLJ height and total thrust) were observed for all streamwise tower loads, however, the amount of correlation varied. The tower base and tower top shear forces all exhibited the pattern to some degree. On the contrary, the bending moments showed a more distinct pattern. This is likely because the bending moments are more sensitive to the wind speed compared to the shear forces. A correlation was also observed between tower base and tower top streamwise loads and the summed thrust force when the LLJ core-speed was above rated wind speed, with the exception of the tower top streamwise bending moment. Although, the pattern of the total thrust force as the LLJ height increased was flipped for the above rated LLJ core-speed case (see Fig. 4.2). Lastly, the tower top streamwise bending moment was likely governed by the mean hub velocity.

The tower base streamwise loads and the tower top streamwise shear force at rated LLJ core-speed all show a decreasing trend with increasing LLJ height. After comparing this trend with the aerodynamic loads on the blades at this core-speed, very little correlation was found. However, it was observed that variation in the aerodynamic loads was large when the LLJ was at 70 m (see Fig. 4.4b), and this might explain why the aforementioned loads showed the largest DEL at this LLJ height. Furthermore, the absolute value of shear both above and below the LLJ core was decreasing as the LLJ height was increasing. This might lead to lower loads as mentioned in section 4.2.2 and Ahmed & Paskyabi (2023).

This wind turbine model in Fig. 3.3 is highly simplified, and only provides a part of the explanation for the observed streamwise tower loads. In reality, a large number of factors are playing a role in the structural loading. This might be the turbulence, the system damping and the floating aspect of this system (i.e. waves and mooring lines). The exact description of the interactions causing the particular patterns in the loading might therefore be difficult to provide. This is also why I did not find a perfect correlation between the aerodynamic loads and

the structural loads. However, the coupling between the aerodynamics and structural loading provides a good baseline, and is likely the most important aspect.

To summarize, I generally noticed a rough correspondance between the LLJ height, the corresponding summed thrust along the blade, and the pattern of how the DEL develops. However, as previously mentioned, the pattern flipped when the pitch control system was fully active at above rated LLJ core-speed. In addition, a contribution from the mean hub velocity was also seen. The results for the tower base loads (for above rated wind speed) did not coincide with results by Gutierrez et al. (2017). In this study, the standard deviation of the tower base streamwise shear force decreased with higher LLJs. This differs from their results. The cause for this is likely the large difference between the research designs (wind turbine, inflow conditions, etc.), however, to the author's knowledge, a closer matched study is not available. Regarding the streamwise bending moment, the results are in better agreement. Although, they attributed their results for this response to modelling. This is likely not the case for the results of this thesis as the pattern is distinct and the uncertainty is small.

4.2.4 Further discussion about spanwise tower loads

Generally, the spanwise loads showed a distinct pattern. The DEL usually increased until the LLJ was at about hub height, afterwards, the DEL decreased as the LLJ height moved upwards. This pattern is found in the how the mean hub velocity changes as the LLJ height increases. Thus, this seems consistent with mode shape 1 for the tower bending, which can govern the tower bending and loads. Further, this pattern roughly corresponded to the sum of the distributed torque force along the blade span. This was likely because the torque force was carried through the blades and to the tower, where it later induced spanwise loads on the tower top and tower base.

For the below rated LLJ core-speed, the aforementioned pattern was observed for the tower base spanwise bending moment, tower top spanwise shear force and tower top spanwise bending moment. Apart from the latter, the values did not alter much as the LLJ height increases. This is however consistent with the torque force and the mean hub

velocity, as they also only varied slightly across the different LLJs. The tower top spanwise bending moment showed a more distinct pattern, and this might be caused by a higher sensitivity to the wind speed and mode shape.

The tower base spanwise shear force for below rated LLJ core-speed was fairly consistent across LLJ heights. However, I did observe a relatively large standard deviation across simulations. Due to the uncertainty of the results, other external forces (e.g. mooring lines and waves) and variations of the mean hub velocity, it was difficult to draw a definite conclusion on the reason behind the consistency.

When the LLJ core-speed was above rated wind speed, the pattern (mentioned in the beginning of the section) was not fully recognized in the tower base spanwise shear force. A plausible explanation might be the uncertainties in the modelling, which was supported by the relatively large standard deviation across simulations in Fig. 4.6c. A similar argument can be made for the tower base spanwise bending moment in Fig. 4.6d.

The spanwise loads are likely also affected by factors other than the torque force and mean hub velocity, such as gyroscopic effects and gravitational effects. Gyroscopic effect is the tendency of a rotating body to turn perpendicular to the rotating axis, and this might induce loads at the tower top. The gravitational effects might result in higher loads due to the mass of the blades. These forces are likely to carry through the structure and cause higher loads.

The results for the spanwise tower base loads (at above rated LLJ core-speed) agrees to some extent with the results in Gutierrez et al. (2017), and the lowest loading (i.e. lowest standard deviation) is often observed when the LLJ is closest to the surface. It is however important to remember that the results don't correlate perfectly, and the uncertainty across different seeds for the spanwise responses is relatively large.

4.3 Blade root loads (for blade 1)

The results for the blade root loads for blade 1 are presented and discussed here. This sub-section is divided into the out-of-plane and

in-plane loads, and the results are analyzed accordingly.

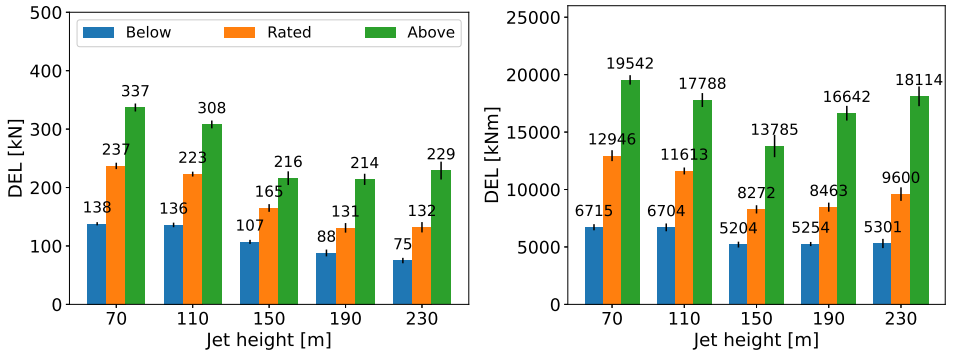

(a) Out-of-plane shear force. (b) Out-of-plane bending moment.

Figure 4.8: Blade root out-of-plane loads for blade 1.

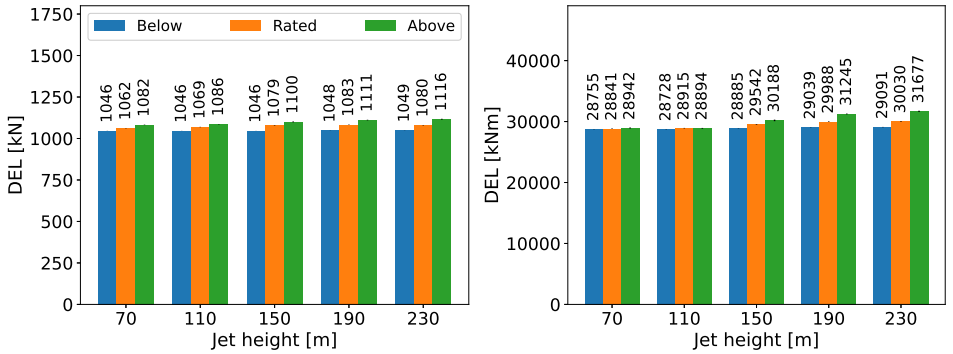

(a) In-plane shear force. (b) In-plane bending moment.

Figure 4.9: Blade root in-plane loads for blade 1. Error bars show 1 standard deviation.

4.3.1 Blade root out-of-plane loads

The blade root out-of-plane shear force at below rated LLJ core-speed shows a step-wise decreasing pattern in Fig. 4.8a. Although, the change in DEL when the LLJ height moved from 70 m to 110 m was insignificant (2 kN). The DEL for the out-of-plane bending moment in Fig. 4.8b stayed essentially equal between 70 m and 110 m LLJ height. However, from LLJ height 110 m to 150 m, the DEL decreased by about 22%. Afterwards, I noticed a slight step-wise increasing pattern. When the

LLJ height increased from 150 m to 230 m, the DEL increased by about 2%.

The blade root out-of-plane shear force at rated LLJ core-speed (in Fig. 4.8a) decreased step-wise from LLJ height 70 m to 190 m. However, the decrease was insignificant for the first step (LLJ height 70 m to 110 m). Additionally the DEL only changed by 1 kN when the LLJ moved from 190 m to 230 m, which is negligible. From Fig. 4.8b, it was observed that the blade root out-of-plane bending moment decreased step-wise from LLJ height 70 m to 150 m. For the last two steps (i.e. LLJ height: 150 m to 190 m and 190 m to 230 m), the DEL showed a slightly increasing trend. The changes in DEL were approx. 36% and 16%, respectively.

The out-of-plane blade shear force at above rated LLJ core-speed (shown in Fig. 4.8a) decreased with the LLJ height until hub height. Thereafter, it showed a slight increase with the LLJ height. The differences correspond to roughly 36% and 6%, respectively. I observed a similar pattern in the evolution of DEL for the out-of-plane blade root bending moment from Fig. 4.8b. However, in this case, the increase in DEL when the LLJ height moved upwards above hub height was more significant. The DEL decreased and increased by about 29% and 31%, respectively.

To get a better understanding of the blade root out-of-plane loads, I applied the simplification mentioned in section 3.1. A wind turbine blade can be simplified as a slender beam with a fixed and a free end. By conceptualizing a distributed force across the slender beam, the structural loads at the fixed end will largely depend on the variation of the distributed force in time. Generally, a larger variation in the distributed force in time results in higher loads at the fixed end. This was precisely displayed by the results of my case study. Figures 4.4a to 4.4c show the standard deviation of the time-dependent thrust force at each blade node. By approximating the area under each graph, which will provide a measure of the total force, and comparing it with the pattern in DEL shown in Figs. 4.8a and 4.8b, a significant correlation was found.

As mentioned in section 4.1, the large variation at the nodes were caused by the LLJ profiles, which contained large gradients in the vertical wind shear. As a blade rotated, the nodes experienced widely

different wind velocities depending on the azimuth (and the associated wind profile). This resulted in large variations in the aerodynamic loads, which was visible in the blade root loading. In addition, as the blade rotates, the centrifugal and rotational forces may push the blades away from the rotational plane, affecting the out-of-plane loads.

Gutierrez et al. (2017) obtained similar results for the in-plane blade root loads as the out-of-plane blade root loads, i.e. no significant changes. However, the results for the out-of-plane loads in this thesis are not consistent with theirs. This is likely due to a combination of several factors. First, the wind turbine model is significantly different: onshore vs offshore (floating) and 1.5 MW vs 15 MW. Second, the LLJ profiles are also significantly different. These factors, along with the differences in turbine specifications and the wind inflow, likely caused the results to be dissimilar.

4.3.2 Blade root in-plane loads

The blade root in-plane loads stayed fairly consistent regardless of LLJ height, and this was true for every LLJ core-speed studied in this thesis. Depending on the LLJ core-speed, it might be argued that the in-plane loads in Fig. 4.9 show a slight increasing trend, however, this was minimal.

This was similar to results obtained by Gutierrez et al. (2017). This likely occurred since the regime of the power curve where the structure resides in for each case was mainly responsible for this consistency. The results revealed a very slight decrease in the loads the closer the LLJ was to the surface, and this might be the main take-away.

At below rated LLJ core-speed, this was likely due to the fact that the rotor was rotating with a similar angular velocity across the LLJ heights, resulting in a similar amount of loading at the blade root. Since the blades are not pitched a significant amount in this regime of the power curve, only the natural blade twist was capturing the wind energy. Additionally, the mean hub velocity was not changing significantly, causing the blades to rotate with a similar angular velocity regardless of LLJ height. The lift and drag are also likely contributing factors, and this might explain any discrepancies.

The explanation for why the blade root in-plane loads stayed similar

when the LLJ core-speed was at rated wind speed was likely controlled by the lift/drag, pitch control and the mean hub velocity. As the mean hub velocity increases, the angular velocity and the lift increases, thus, the loads will increase. However, in this case, the loads stayed similar. A likely explanation might be that the drag and pitch control system was regulating the damage on the blade roots. Although, it might be difficult to perfectly explain the interactions that are causing this, especially since there are other factors contributing such as the waves, mooring lines and damping.

Lastly, when the LLJ core-speed was at above rated wind speed, this was likely caused by the interactions between the torque force and the blade pitch. As the torque increases, the control system had to increase the blade pitch to control the rotational velocity of the blades. This resulted in the rotational velocity of the blades being similar across LLJ heights along with the in-plane loads. Additionally, the lift and drag force plays a role in the in-plane blade root loads, which might explain any discrepancies.

4.4 Limitations

The limitations of this thesis are described here. The section mentions limitations of the modelling software, limitations of the choices of the author and limitations of the current framework of turbulence.

The standard deviation of turbulent fluctuations in TurbSim is considered to be similar across the grid. Hence, the TI is only dependent on the local wind velocity. Thus, the shape of the LLJ profile results in the TI increasing after the LLJ peak when the mean wind velocity is decreasing. This is atypical since the TI above the peak is expected to decrease due to the stable conditions. Still, this result is not unphysical, as it has been observed before by Schepers et al. (2021).

In OpenFAST, the user has the choice to use either stable or unstable aerodynamics. Due to unstable aerodynamics turning off for specific nodes along the blade, it was decided to turn off unstable aerodynamics all together. This likely causes the wind turbine loads to be under-predicted, since the effects of the turbulent wake region behind the blade is not considered. However, since the thesis was interested in the

differences rather than the absolute values, the results would likely not change even if the unsteady aerodynamics were turned on.

The turbulence boxes in this thesis were generated using mathematical models and parameterized variables rather than observational data. Since the wind conditions and wave conditions are often site specific (Ma et al., 2019), the absolute values for the DEL might not be representative for an actual wind farm site.

The current theoretical framework of turbulence modelling is based on micro-scale turbulence and surface layer scaling. However, due to the large scale of current wind turbines, this might not be sufficient to estimate structural loading, particularly for atypical atmospheric conditions such as a LLJ event. This is an inherent problem of current turbulence modelling, and not necessarily particular for this thesis. In addition, the turbulence is assumed as Gaussian. A study by Berg et al. (2016) found that the loads (both extreme and fatigue) caused non-Gaussian turbulence is not significantly different from Gaussian turbulence. Although, the authors utilized a 5 MW land-based wind turbine, and the effects on a 15 MW floating wind turbine might or might not be different.

The thesis only considered a single floating wind turbine. In reality, the wind turbine is likely placed inside a wind farm, and the inflow wind is much more turbulent.

Chapter 5

Conclusions and Future Work

The thesis studied the effects of the Low-Level Jet (LLJ) height and the accompanying shape on the structural loading of a 15 MW floating wind turbine. It also briefly discussed how the aerodynamic loads were affected to get a better understanding of the structural loads. 15 case studies were performed with five LLJs at three different core-speeds using TurbSim and OpenFAST.

The results revealed that the interactions between structure and wind profile were not trivial, and there is no singular pattern on how the loads develop as the LLJ height increases. However, it was observed that the structural loads are related to the aerodynamic loads, the mean hub velocity and the shear of the profile.

The wind speed at hub height was highest when the LLJ was at hub height, and decreased when the LLJ moved upwards or downwards. However, the decrease was not symmetrical due to the shape of the profiles. This effect (i.e. change in mean hub velocity) seemed to have an affect on most of the load responses.

The mean distributed aerodynamic loads were affected by the shear of the wind profile, the wind speed at hub height and the extent of response from the control system. It was noticed that the slope of the mean distribution was largest when the LLJ was at hub height and the aerodynamic load variations at the nodes along the blade were particularly affected by the profile. In addition, the total thrust and torque was largest when the LLJ was at hub height. The variations were the largest when the LLJ was closest to the surface due to the

vertical wind shear.

The least affected load parameter was the blade root in-plane loads, and they stayed fairly consistent. This was due to a combination of blade design, wind speed and the control system (depending on the LLJ core-speed). On the contrary, the out-of-plane blade root loads were significantly affected. This was mainly due to the large amount of variation in the aerodynamic loads caused by the different LLJ shapes at different heights, which was present regardless of LLJ core-speed. Generally, the lowest out-of-plane loads were observed when the LLJ was at hub height.

The streamwise loads were often related to the total thrust and the mean hub velocity (which governs the tower bending). The total thrust was related to the LLJ height and the accompanying shape. This is because the thrust and the wind at hub height acts as a pushing force on the tower, causing the loads at the tower top and tower base. Additionally, the shear in the wind profile also seem to have an affect. The spanwise loads seem to be related to the mean hub velocity, which governs the bending of the tower, and the summed torque force, which is passed to the tower through the shaft. The error between simulations was also usually larger for the spanwise loads compared to streamwise loads. Lastly, the results also showed that the loads were affected by the absolute value of shear in the wind profile.

To the author's knowledge, the field of LLJs and their effects on a wind turbine has not been widely studied, and this thesis serves as a starting point for future work. In future studies, I recommend: more case studies with larger number of LLJ core-speeds and heights, the use of observational data for generating wind fields, the use of higher fidelity models and the inclusion of wind farm effects. Furthermore, the theoretical framework of turbulence modelling is outdated with regards to the large scale of newer wind turbines, particularly for atypical processes such as LLJ events. Therefore, work on turbulence modelling is recommended.

Bibliography

Ahmed, F. M., & Paskyabi, M. B. (2023). Effects of negative shear on loads for a 15 MW offshore wind turbine during low-level jet events (under review). *Journal of Physics: Conference Series*, .

Allen, C., Viselli, A., Dagher, H., Goupee, A., Gaertner, E., Abbas, N., Hall, M., & Barter, G. (2020). *Definition of the UMaine VolturnUS-S Reference Platform Developed for the IEA Wind 15-Megawatt Offshore Reference Wind Turbine*. Technical Report NREL.

Archer, C. L., & Jacobson, M. Z. (2005). Evaluation of global wind power. *Journal of Geophysical Research*, *110*.

Bendat, J. S., & Piersol, A. G. (1980). *Engineering applications of correlation and spectral analysis*. New York, United States: John Wiley & Sons, Inc.

Benitz, M. A., Lackner, M. A., & Schmidt, D. P. (2015). Hydrodynamics of offshore structures with specific focus on wind energy applications. *Renewable and Sustainable Energy Reviews*, *44*, 692–716.

Berg, J., Natarajan, A., Mann, J., & Patton, E. G. (2016). Gaussian vs non-Gaussian turbulence: impact on wind turbine loads. *Wind Energy*, *19*, 1975–1989.

Betz, A. (1920). Das Maximum der theoretisch möglichen Ausnützung des Windes durch Windmotoren. *Zeitschrift für das gesamte Turbinenwesen*, *26*, 307–309.

Blackadar, A. K. (1957). Boundary Layer Wind Maxima and Their Significance for the Growth of Nocturnal Inversions. *Bulletin of the American Meteorological Society*, *38*, 283–290.

Breton, S. P., & Moe, G. (2009). Status, plans and technologies for offshore wind turbines in Europe and North America. *Renewable Energy*, *34*, 646–654.

Businger, J. A., Wingard, J. C., Izumi, Y., & Bradley, E. F. (1971). Flux-Profile Relationships in the Atmospheric Boundary Layer. *Journal of the Atmospheric Sciences*, *28*, 181–189.

Carter, D. J. (1982). Prediction of wave height and period for a constant wind velocity using the JONSWAP results. *Ocean Engineering*, *9*, 17–33.

Charnock, H. (1955). Wind stress on a water surface. *Quarterly Journal of the Royal Meteorological Society*, *81*, 639–640.

Cheynet, E., & Jakobsen, J. B. (2022). *Wind load on structures. Part 1.*. Lecture notes in ENERGI322, University of Bergen.

Cheynet, E., Jakobsen, J. B., & Reuder, J. (2018). Velocity Spectra and Coherence Estimates in the Marine Atmospheric Boundary Layer. *Boundary-Layer Meteorology*, *169*, 429–460.

Cheynet, E., Jakobsen, J. B., Snæbjörnsson, J., Mann, J., Courtney, M., Guillaume, L., & Svardal, B. (2017). Measurements of Surface-Layer Turbulence in a Wide Norwegian Fjord Using Synchronized Long-Range Doppler Wind Lidars. *Remote Sensing*, *9*.

Davenport, A. G. (1961). The spectrum of horizontal gustiness near the ground in high winds. *Quarterly Journal of the Royal Meteorological Society*, *87*, 194–211.

EERE (2022). Wind Turbines: the Bigger, the Better. URL: `https://www.energy.gov/eere/articles/wind-turbines-bigger-better`.

Ehrlich, R. (2013). *Renewable Energy: A First Course*. Boca Raton, Florida, United States: CRC Press.

European Committee for Standardization (1991). *EN 1991-1-4: Eurocode 1 - Wind actions*. Technical Report European Committee for Standardization.

Frandsen, S., & Christensen, C. J. (1994). Structural Loads in Large Wind Farm Arrays. In G. C. Larsen (Ed.), *Contributions from the Department of Meteorology and Wind Energy to the EWEC'94 Conference in Thessaloniki, Greece.*

Frost, R. (1948). Atmospheric turbulence. *Quarterly Journal of the Royal Meteorological Society*, *74*, 316–338.

Gaertner, E., Rinker, J., Sethuraman, L., Anderson, B., Zahle, F., & Barter, G. (2020). *IEA Wind TCP Task 37: Definition of the IEA 15 MW Offshore Reference Wind Turbine.* Technical Report International Energy Agency.

Guest, P., Persson, P. O. G., Wang, S., Jordan, M., Jin, Y., Blomquist, B., & Fairall, C. (2018). Low-Level Baroclinic Jets Over the New Arctic Ocean. *Journal of Geophysical Research. Oceans*, *123*, 4074–4091.

Gutierrez, W., Araya, G., Basu, S., Ruiz-Columbie, A., & Castillo, L. (2014). Toward understanding low level jet climatology over west Texas and its impact on wind energy. *Journal of Physics: Conference Series*, *524*.

Gutierrez, W., Ruiz-Columbie, A., Tutkun, M., & Castillo, L. (2017). Impacts of the low-level jet's negative wind shear on the wind turbine. *Wind Energy Science*, *2*, 533–545.

Hasselmann, K. F., Barnett, T. P., Bouws, E., Carlson, H., Cartwright, D. E., Eake, K., Euring, J., Gicnapp, A., Hasselmann, D., & Kruseman, P. (1973). Measurements of wind-wave growth and swell decay during the joint North Sea wave project (JONSWAP). *Deutschen Hydrographischen Zeitschrift*, *8*.

Holthuijsen, L. H. (2007). *Waves in Oceanic and Coastal Waters.* Cambridge University Press.

Holton, J. R. (1967). The diurnal boundary layer wind oscillation above sloping terrain. *Tellus A: Dynamic Meteorology and Oceanography*, *19*, 199–205.

Hsu, S. A., Meindl, E. A., & Gilhousen, D. B. (1994). Determining the power-law wind-profile exponent under near-neutral stability conditions at sea. *Journal of Applied Meteorology*, *33*, 757–765.

IEA (2022). Wind Electricity. URL: `https://www.iea.org/reports/wind-electricity`.

IEC (2015). *IEC TS 61400-13: Wind Turbines - Part 13: Measurement of mechanical loads*. Technical Report IEC.

Jiang, Q., Wang, S., & O'Neill, L. (2010). Some Insights into the Characteristics and Dynamics of the Chilean Low-Level Coastal Jet. *Monthly Weather Review*, *138*, 3185–3206.

Jonkman, B., & Jonkman, J. (2016). *FAST v8.16.00a-bjj*. Technical Report NREL.

Jonkman, B. J. (2014). *TurbSim User's Guide v2.00.00*. Technical Report NREL.

Jonkman, J. M. (2009). Dynamics of offshore floating wind turbines-model development and verification. *Wind Energy*, *12*, 459–492.

Jonkman, J. M., & Buhl, M. L. (2005). *FAST User's Guide*. Technical Report NREL.

Jonkman, J. M., Hayman, G. J., Jonkman, B. J., Damiani, R. R., & Murray, R. E. (2017). *AeroDyn v15 User's Guide and Theory Manual*. Technical Report NREL.

Kaimal, J. C., & Finnigan, J. J. (1994). *Atmospheric Boundary Layer Flows : Their Structure and Measurement*. Oxford University Press.

Kaimal, J. C., Wyngaard, J. C., Izumi, Y., & Coté, O. R. (1972). Spectral characteristics of surface-layer turbulence. *Quarterly Journal of the Royal Meteorological Society*, *98*, 563–589.

Kundu, P. K., Cohen, I. M., & Dowling, D. R. (2016). *Fluid Mechanics*. (6th ed.). Academic Press.

Letcher, T. M. (2017). *Wind Energy Engineering : A Handbook for Onshore and Offshore Wind Turbines*. Elsevier Science & Technology.

Ma, K.-T., Luo, Y., Kwan, T., & Wu, Y. (2019). *Mooring System Engineering for Offshore Structures*. Elsevier Science & Technology.

Massel, S. R. (1996). *Ocean Surface Waves: Their Physics and Prediction*. World Scientific Publishing Co. Pte. Ltd.

Matsuishi, M., & Endo, T. (1968). Fatigue of metals subjected to varying stress. *Japan Society of Mechanical Engineering*, .

Monin, A. S., & Obukhov, A. M. (1954). Basic Laws of Turbulent Mixing in the Surface Layer of the Atmosphere. *Trans. Geophys. Inst. Akad., Nauk USSR*, *151*, 163–187.

Morison, J. R., O'Brien, M. P., Johnson, J. W., & Schaaf, S. A. (1950). The force exerted by surface waves on piles. *Journal of Petroleum Technology*, *189*, 149–157.

Newman, J. F., & Klein, P. M. (2014). The Impacts of Atmospheric Stability on the Accuracy of Wind Speed Extrapolation Methods. *Resources*, *3*, 81–105.

Nielsen, F. G. (2021). *FLOATING SUPPORT STRUCTURES*. Lecture notes in ENERGI321, University of Bergen.

NREL (2023). OpenFAST Documentation — OpenFAST v3.4.1 documentation. URL: `https://openfast.readthedocs.io/en/main/`.

Nybø, A., Nielsen, F. G., & Godvik, M. (2021). Quasi-static response of a bottom-fixed wind turbine subject to various incident wind fields. *Wind Energy*, (pp. 1482–1500).

Panofsky, H. A., & Dutton, J. A. (1984). *Atmospheric Turbulence: Models and Methods for Engineering Applications*. John Wiley & Sons Inc.

Paskyabi, M. B., Bui, H., & Penchah, M. M. (2022). Atmospheric-Wave Multi-Scale Flow Modelling. *HIPERWIND project*, (p. 131).

Petersen, E. L., Mortensen, N. G., Landberg, L., Højstrup, J., & Frank, H. P. (1998). Wind power meteorology. Part I: climate and turbulence. *Wind Energy*, *1*, 25–45.

Pichugina, Y. L., Brewer, W. A., Banta, R. M., Choukulkar, A., Clack, C. T. M., Marquis, M. C., McCarty, B. J., Weickmann, A. M., Sandberg, S. P., Marchbanks, R. D., & Hardesty, R. M. (2017). Properties of the Offshore Low Level Jet and Rotor Layer Wind Shear as Measured by Scanning Doppler Lidar. *Wind Energy*, *20*, 943–1127.

Pielke, R. A., & Panofsky, H. A. (1970). Turbulence characteristics along several towers. *Boundary-Layer Meteorology*, *1*, 115–130.

Platt, A., Jonkman, B., & Jonkman, J. (2016). *InflowWind User's Guide*. Technical Report NREL.

Putri, R. M., Cheynet, E., Obhrai, C., & Jakobsen, J. B. (2022). Turbulence in a coastal environment: the case of Vindeby. *Wind Energy Science*, *7*, 1693–1710.

Roithmayr, C. M., & Hodges, D. H. (2016). *Dynamics: Theory and Application of Kane's Method*. Cambridge University Press.

Ropelewski, C. F., Tennekes, H., & Panofsky, H. A. (1973). Horizontal coherence of wind fluctuations. *Boundary-Layer Meteorology*, *5*, 353–363.

Schepers, G., Dorp, P. V., Verzijlbergh, R., Baas, P., & Jonker, H. (2021). Aeroelastic loads on a 10 MW turbine exposed to extreme events selected from a year-long large-eddy simulation over the North Sea. *Wind Energy Science*, *6*, 983–996.

Stull, R. B. (1988). *An Introduction to Boundary Layer Meteorology*. (1st ed.). Dordrecht, The Netherlands: Kluwer Academic Publishers.

Sverdrup, H. U., & Munk, W. H. (1947). *Wind, sea, and swell; theory of relations for forecasting*. U.S. Navy Hydrographic Office.

Tong, C. (1996). TAYLOR'S HYPOTHESIS AND TWO-POINT COHERENCE MEASUREMENTS. *Boundary-Layer Meterology*, *81*, 399–410.

Wagner, D., Steinfeld, G., Witha, B., Wurps, H., & Reuder, J. (2019). Low level jets over the southern North Sea. *Meteorologische Zeitschrift*, *28*, 389–415.

Watson, B. H. H. (1975). *A study of the statistical approach to wind loading*. Master's thesis University of Cape Town.

Wu, J. (1980). Wind-Stress Coefficients over Sea Surface near Neutral Conditions - A Revisit. *Journal of Physical Oceanograhy*, *10*, 727–740.

Zhang, X., Yang, C., & Li, S. (2019). Influence of Low-Level Jet intensity on aerodynamic loads of horizontal axis wind turbine rotor. *Engineering Applications of Computational Fluid Mechanics*, *13*, 300–308.